



# Universal Scaling Laws for Solar and Stellar Atmospheric Heating: Catalog of Power-law Index between Solar Activity Proxies and Various Spectral Irradiances

Shin Toriumi<sup>1</sup> , Vladimir S. Airapetian<sup>2,3</sup> , Kosuke Namekata<sup>4</sup> , and Yuta Notsu<sup>5,6,7</sup> <sup>1</sup> Institute of Space and Astronautical Science, Japan Aerospace Exploration Agency, 3-1-1 Yoshinodai, Chuo-ku, Sagami-hara, Kanagawa 252-5210, Japan  
[toriumi.shin@jaxa.jp](mailto:toriumi.shin@jaxa.jp)<sup>2</sup> Sellers Exoplanetary Environments Collaboration, NASA Goddard Space Flight Center, Greenbelt, MD, USA<sup>3</sup> Department of Physics, American University, Washington, DC, USA<sup>4</sup> National Astronomical Observatory of Japan, 2-21-1 Osawa, Mitaka, Tokyo 181-8588, Japan<sup>5</sup> Laboratory for Atmospheric and Space Physics, University of Colorado Boulder, 3665 Discovery Drive, Boulder, CO 80303, USA<sup>6</sup> National Solar Observatory, 3665 Discovery Drive, Boulder, CO 80303, USA<sup>7</sup> Department of Earth and Planetary Sciences, Tokyo Institute of Technology, 2-12-1 Ookayama, Meguro-ku, Tokyo 152-8551, Japan

Received 2022 June 22; revised 2022 August 13; accepted 2022 August 17; published 2022 September 30

## Abstract

The formation of extremely hot outer atmospheres is one of the most prominent manifestations of magnetic activity common to late-type dwarf stars, including the Sun. It is widely believed that these atmospheric layers, the corona, transition region, and chromosphere, are heated by the dissipation of energy transported upwards from the stellar surface by the magnetic field. This is signified by the spectral line fluxes at various wavelengths, scaled with power-law relationships against the surface magnetic flux over a wide range of formation temperatures, which are universal to the Sun and Sunlike stars of different ages and activity levels. This study describes a catalog of power-law indices between solar activity proxies and various spectral line fluxes. Compared to previous studies, we expanded the number of proxies, which now includes the total magnetic flux, total sunspot number, total sunspot area, and the F10.7 cm radio flux, and further enhanced the number of spectral lines by a factor of 2. This provides the data to study in detail the flux–flux scaling laws from the regions specified by the temperatures of the corona ( $\log(T/K) = 6-7$ ) to those of the chromosphere ( $\log(T/K) \sim 4$ ), as well as the reconstruction of various spectral line fluxes of the Sun in the past, F-, G-, and K-type dwarfs, and the modeled stars.

*Unified Astronomy Thesaurus concepts:* [Stellar coronae \(305\)](#); [Stellar chromospheres \(230\)](#); [Solar spectral irradiance \(1501\)](#); [Solar corona \(1483\)](#); [Solar transition region \(1532\)](#); [Solar chromosphere \(1479\)](#); [Solar magnetic fields \(1503\)](#); [Solar analogs \(1941\)](#); [G dwarf stars \(556\)](#)

## 1. Introduction

Late-type dwarf stars, including the Sun, commonly exhibit magnetic activity in a variety of forms. In their turbulent outermost envelope, the convection zone, magnetic flux is generated and enhanced by the dynamo mechanism (Brun & Browning 2017; Charbonneau 2020; Fan 2021). The produced magnetic flux emerges in the photosphere and builds up active regions, including sunspots/starspots (Solanki 2003; Berdyugina 2005; Strassmeier 2009; Cheung & Isobe 2014; Toriumi 2014). Active regions contain highly concentrated magnetic flux that drives eruptive processes such as flares and coronal mass ejections via magnetic reconnection (Benz & Güdel 2010; Fletcher et al. 2011; Shibata & Magara 2011; Maehara et al. 2012; Davenport 2016; Benz 2017; Toriumi et al. 2017; Toriumi & Wang 2019), and coronal mass ejections accompanying flares expand into interplanetary space (Collier Cameron & Robinson 1989; Chen 2011; Harra et al. 2016; Veronig et al. 2021; Namekata et al. 2021). It is widely believed that the magnetic flux covering the entire stellar surface transports the energy from the surface upwards and heats the outer stellar atmospheres, known as the chromosphere, transition region, and corona (Güdel 2004). However, the exact mechanism of atmospheric heating is still unclear (Klimchuk 2006).

The comparison between the full-disk magnetograms and the associated X-ray and extreme ultraviolet (EUV) images of the Sun clearly shows that the rate of atmospheric heating strongly depends on the surface magnetic flux. Empirical relationships between the surface magnetic flux and quasi-steady X-ray emission flux of the Sun and Sunlike stars have been well characterized as a function of the rotation period and average magnetic field strength. For example, by measuring the total unsigned magnetic flux ( $\Phi$ ) and X-ray flux ( $F_X$ ) of various structures such as the quiet Sun, X-ray bright points, active regions, entire solar disk, G, K, M dwarfs, and T Tauri stars, Pevtsov et al. (2003) found that the two parameters showed a power-law scaling with a power-law index in excess of unity,  $F_X \propto \Phi^\alpha$ , where  $\alpha = 1.15$ . Similar values ( $\alpha \gtrsim 1$ ) were obtained by other studies (Fisher et al. 1998; Vidotto et al. 2014; Reiners et al. 2022). It was found that the X-ray flux of late-type dwarf stars decreases with the rotation period or the Rossby number  $Ro$  (defined as the rotation period divided by the convective turnover time: Noyes et al. 1984) in the regime of  $Ro \gtrsim 0.1$ , while it is saturated for  $Ro \lesssim 0.1$  (Pizzolato et al. 2003; Wright et al. 2011; Vidotto et al. 2014; Reiners et al. 2014; Takasao et al. 2020). Recently, studies also investigated the dependence of magnetic field strength on  $Ro$  (Reiners et al. 2022).

These relationships can be attributed to stellar evolution (Skumanich 1972). The rotation speed, which is fastest immediately after star birth, determines the efficiency of the stellar dynamo, and hence, the average magnetic field strength and X-ray luminosity are driven by the magnetic heating of the corona. As the stellar evolution progresses, the stellar wind

driven by the magnetic field carries away the angular momentum, which decreases the rotation speed. As a result, the dynamo action, average field strength, and X-ray luminosity weaken. For detailed discussions on the stellar evolution and activity, see reviews by Güdel (2007), Testa et al. (2015), Brun & Browning (2017), and Vidotto (2021).

High-energy radiation can create detrimental conditions for the habitability of exoplanets around active host stars. Specifically, the X-ray and EUV radiations, collectively referred to as XUV, emitted from active regions and stellar flares can evaporate the planetary atmospheres by the photoionization-driven heating that expands the exosphere, thereby igniting ionospheric and hydrodynamic escape. Therefore, investigating the dependence of spectral line irradiances on the stellar magnetic activity is important for elucidating the stellar atmospheric heating as well as understanding their effects on exoplanets (Linsky 2019; Airapetian et al. 2020).

Despite its importance for the exoplanetary atmospheric evolution and habitability, it is difficult to observe stellar EUV flux, especially of wavelengths longer than 360 Å owing to the strong absorption by the interstellar medium (see, e.g., Cruddace et al. (1974) for absorption cross-section). Therefore, the EUV spectrum is estimated and reproduced by using the scaling laws between EUV and other observable wavelengths, such as X-ray and Ca II K, or by obtaining the differential emission measure distributions (Sanz-Forcada et al. 2011; Linsky et al. 2014; Chadney et al. 2015; Youngblood et al. 2016, 2017; Ayres 2020, 2021; Johnstone et al. 2021). However, considering that stellar atmospheric heating is moderated by the surface magnetic field, physical correspondence can be obtained directly by measuring the scaling relations between irradiances and the surface magnetic flux.

Accordingly, (Toriumi & Airapetian 2022, hereafter TA22) derived the power-law correlations between the total unsigned magnetic flux of the Sun over 10 years and the irradiances of emission lines of various wavelengths, i.e., various temperature domains. As a result, it was found that the acquired correlations were strikingly replicated in Sunlike G-type stars at five spectral lines: X-rays, Fe XV 284 Å, C II 1335 Å, Ly $\alpha$ , and Mg II h and k. This indicated that the extremely hot outer atmospheres of the Sun and Sunlike stars are heated by a common mechanism, which is independent of the stellar age or activity level.

The obtained power-law index for the soft X-ray band in TA22,  $\alpha = 1.16 \pm 0.03$ , is highly consistent with the preceding studies by, e.g., Pevtsov et al. (2003), wherein the exponent was  $\alpha = 1.15$ . Furthermore, we found that the other coronal line fluxes can be consistently scaled with the above-unity exponents. Such values have been explained using theoretical models based on RTV scaling laws (Fisher et al. 1998; Zhuleku et al. 2020; Takasao et al. 2020) and numerical simulations, wherein Alfvén waves propagating in the corona loop heat the atmosphere via turbulent dissipation (Shoda & Takasao 2021). For chromospheric lines, the  $\alpha$  values lie below unity in TA22, which is in agreement with previous studies (Skumanich et al. 1975; Schrijver et al. 1989; Harvey & White 1999; Rezaei et al. 2007; Barczynski et al. 2018).

In TA22, we examined the correlations of multiple lines to the total unsigned magnetic flux of the Sun and compared them with the stellar observations. However, by expanding the activity proxy to the historical records of sunspot number, sunspot area, and the F10.7 cm radio flux, and by further enhancing the number of lines to be investigated, we can provide the means to synthesize the

spectral irradiances over a wide range of wavelength, based on the combination of the obtained power-law indices and proxies of the Sun in the past, other Sunlike stars, and numerical models. Therefore, in this study, we create a catalog of power-law scaling factors for various lines and activity proxies by analyzing solar synoptic observations. Considering the number of lines was particularly small for the transition region temperatures in TA22, this study also leads to a better understanding of how  $\alpha$  changes as the temperature changes from the chromosphere to the corona.

In Section 2, we provide detailed descriptions of the data that are analyzed, while Section 3 explains how we measure the power-law correlations. Section 4 provides the catalog of the power-law index. We show the temperature and wavelength dependence of the power-law index in Section 5 based on the obtained scalings and demonstrate how to synthesize the line and band irradiances in Section 6. Finally, Section 7 summarizes and discusses the implications of the obtained results.

## 2. Data

In this study, we investigated the thermal responses of upper atmospheres to the magnetic flux on the surface by comparing the light curves of spectral lines and bands of various wavelengths, or various formation temperatures, with multiple proxy data representing the solar magnetic activity. As proxies, we adopted two kinds of the total unsigned magnetic flux, both of which were derived from the line-of-sight (LOS) magnetic field, total sunspot number, total sunspot area, and the F10.7 cm radio flux between 2010 May and 2020 February.

Table 1 summarizes the key information of the proxies and spectral lines/bands, such as the formation temperature, central wavelength and spectral window for calculating the irradiance, and the data source. All spectral irradiances were converted to values at 1 au. The F10.7 cm flux was used both as a proxy of solar activity and as a light curve data representing the solar atmospheres.

### 2.1. SDO/HMI

To calculate the total unsigned magnetic flux in the visible hemisphere of the Sun, we used the full-disk magnetograms obtained by the Helioseismic and Magnetic Imager (HMI; Scherrer et al. 2012; Schou et al. 2012) on board the Solar Dynamics Observatory (SDO), which was launched in 2010 February and began observations in 2010 May. This determines the beginning of the target period in this study.

HMI obtains full-disk continuum images, magnetograms, and Dopplergrams with cadences of 45 s and 720 s by acquiring the spectropolarimetric signals of the Fe I 6173.3 Å line. In this study, we analyzed four LOS magnetograms of 720 s cadence at 0, 6, 12, and 18 UT for each day, which were reduced from the original  $4096 \times 4096$  pixels to  $1024 \times 1024$  pixels by averaging over a  $4 \times 4$  pixel tile.<sup>8</sup> By integrating the LOS field strength  $B_{\text{LOS}}$  over the entire solar disk, two types of total magnetic flux were obtained. One is the radial unsigned magnetic flux, wherein the radial field strength at each pixel, which is estimated by correcting the viewing angle from the disk center ( $\theta$ ),  $B_{\text{LOS}}/\cos\theta$ , is integrated over the disk,  $\Phi_{\text{rad}} = \int |B_{\text{LOS}}/\cos\theta| dS$ . The other is the LOS unsigned magnetic flux, where the LOS field strength is simply integrated over the disk,  $\Phi_{\text{LOS}} = \int |B_{\text{LOS}}| dS$ . In both cases, the noise levels were

<sup>8</sup> <http://jsoc.stanford.edu/data/hmi/fits>

**Table 1**  
Summary of the Observables

Feature (1)	$\log(T/K)$ (2)	Wavelength ( $\text{\AA}$ ) (3)	Basal (4)	Minimum (5)	Maximum (6)	Unit (7)	Source (8)
Radial magnetic flux	3.8	6173.3	$1.18 \times 10^{23}$	$1.16 \times 10^{23}$	$3.35 \times 10^{23}$	Mx	SDO/HMI
LOS magnetic flux	3.8	6173.3	$7.02 \times 10^{22}$	$6.85 \times 10^{22}$	$2.52 \times 10^{23}$	Mx	SDO/HMI
Sunspot number	3.8	WL	0	0	220	...	WDC-SILSO (ver 2.0)
Sunspot area	3.8	WL	0	0	3120	MSH	USAF/NOAA
F10.7 cm radio	$\sim 6$	$10.7 \times 10^8$	68.83	63.67	466.57	sfu	DRAO
Total solar irradiance	3.8	WL	...	1358.5	1362.3	$\text{W m}^{-2}$	SORCE/TIM
X-rays 1–8 $\text{\AA}$	6–7	1–8	0	$1.00 \times 10^{-9}$	$4.81 \times 10^{-5}$	$\text{W m}^{-2}$	GOES/XRS
X-rays 5.2–124 $\text{\AA}$	6–7	5.2–124	$2.11 \times 10^{-4}$	$1.85 \times 10^{-4}$	$1.01 \times 10^{-3}$	$\text{W m}^{-2}$	SORCE/XPS
Fe XV 284 $\text{\AA}$	6.4	$284.15 \pm 1.50$	$9.36 \times 10^{-6}$	$5.68 \times 10^{-6}$	$1.27 \times 10^{-4}$	$\text{W m}^{-2}$	SORCE/XPS
Fe XIV 211 $\text{\AA}$	6.3	$211.32 \pm 1.50$	$1.20 \times 10^{-5}$	$9.88 \times 10^{-6}$	$6.75 \times 10^{-5}$	$\text{W m}^{-2}$	SORCE/XPS
X-rays (XRT)	$6.2 \pm 0.1$	5–60	$5.00 \times 10^{-5}$	$4.71 \times 10^{-5}$	$1.01 \times 10^{-3}$	$\text{W m}^{-2}$	Hinode/XRT
Fe XII 193+195 $\text{\AA}$	6.2	$193.50 \pm 2.50$	$6.16 \times 10^{-5}$	$5.66 \times 10^{-5}$	$1.72 \times 10^{-4}$	$\text{W m}^{-2}$	SORCE/XPS
Fe XII 1349 $\text{\AA}$	6.2	$1349.40 \pm 1.00$	$3.64 \times 10^{-6}$	$3.23 \times 10^{-6}$	$5.66 \times 10^{-6}$	$\text{W m}^{-2}$	SORCE/SOLSTICE
Fe X 174 $\text{\AA}$	6.1	$174.53 \pm 1.50$	$5.64 \times 10^{-5}$	$5.40 \times 10^{-5}$	$0.90 \times 10^{-4}$	$\text{W m}^{-2}$	SORCE/XPS
Fe XI 180 $\text{\AA}$	6.1	$180.41 \pm 1.50$	$4.57 \times 10^{-5}$	$4.31 \times 10^{-5}$	$0.95 \times 10^{-4}$	$\text{W m}^{-2}$	SORCE/XPS
F10.7 cm radio	$\sim 6$	$10.7 \times 10^8$	68.83	63.67	466.57	sfu	DRAO
Fe IX 171 $\text{\AA}$	5.9	$171.07 \pm 1.50$	$5.50 \times 10^{-5}$	$5.32 \times 10^{-5}$	$0.73 \times 10^{-4}$	$\text{W m}^{-2}$	SORCE/XPS
N V 1238 $\text{\AA}$	5.3	$1238.90 \pm 1.15$	$1.62 \times 10^{-5}$	$1.55 \times 10^{-5}$	$2.39 \times 10^{-5}$	$\text{W m}^{-2}$	SORCE/SOLSTICE
N V 1242 $\text{\AA}$	5.3	$1242.95 \pm 1.00$	$1.04 \times 10^{-5}$	$9.89 \times 10^{-6}$	$1.54 \times 10^{-5}$	$\text{W m}^{-2}$	SORCE/SOLSTICE
C IV 1548 $\text{\AA}$	5.1	$1548.25 \pm 1.20$	$1.11 \times 10^{-4}$	$1.07 \times 10^{-4}$	$1.53 \times 10^{-4}$	$\text{W m}^{-2}$	SORCE/SOLSTICE
C IV 1551 $\text{\AA}$	5.1	$1550.73 \pm 0.95$	$6.58 \times 10^{-5}$	$6.38 \times 10^{-5}$	$9.02 \times 10^{-5}$	$\text{W m}^{-2}$	SORCE/SOLSTICE
C III 1175 $\text{\AA}$	5.0	$1175.70 \pm 1.75$	$5.52 \times 10^{-5}$	$5.35 \times 10^{-5}$	$8.24 \times 10^{-5}$	$\text{W m}^{-2}$	SORCE/SOLSTICE
He II 256 $\text{\AA}$ +blends	4.9	$256.30 \pm 3.00$	$5.53 \times 10^{-5}$	$5.20 \times 10^{-5}$	$1.21 \times 10^{-4}$	$\text{W m}^{-2}$	SORCE/XPS
He II 304 $\text{\AA}$	4.9	$304.00 \pm 1.00$	$4.25 \times 10^{-4}$	$4.09 \times 10^{-4}$	$6.19 \times 10^{-4}$	$\text{W m}^{-2}$	SORCE/XPS
Si IV 1393 $\text{\AA}$	4.9	$1393.85 \pm 1.30$	$4.45 \times 10^{-5}$	$4.27 \times 10^{-5}$	$7.66 \times 10^{-5}$	$\text{W m}^{-2}$	SORCE/SOLSTICE
Si IV 1402 $\text{\AA}$	4.9	$1402.85 \pm 0.85$	$2.32 \times 10^{-5}$	$2.25 \times 10^{-5}$	$3.91 \times 10^{-5}$	$\text{W m}^{-2}$	SORCE/SOLSTICE
Si III 1206 $\text{\AA}$	4.8	$1206.60 \pm 1.25$	$8.59 \times 10^{-5}$	$8.32 \times 10^{-5}$	$1.66 \times 10^{-4}$	$\text{W m}^{-2}$	SORCE/SOLSTICE
He I 10830 $\text{\AA}$	4.5	$10830.40 \pm 0.25$	0.0292	0.0270	0.0308	$\text{W m}^{-2}$	SORCE/SIM & SOLIS/ISS
C II 1335 $\text{\AA}$	4.3	$1335.25 \pm 1.90$	$1.57 \times 10^{-4}$	$1.52 \times 10^{-4}$	$2.46 \times 10^{-4}$	$\text{W m}^{-2}$	SORCE/SOLSTICE
H I 1216 $\text{\AA}$ ( $\text{Ly}\alpha$ )	4.3	$1215.70 \pm 2.00$	$5.73 \times 10^{-3}$	$5.60 \times 10^{-3}$	$8.94 \times 10^{-3}$	$\text{W m}^{-2}$	SORCE/SOLSTICE
O I 1302 $\text{\AA}$	4.2	$1302.20 \pm 0.85$	$4.16 \times 10^{-5}$	$3.93 \times 10^{-5}$	$5.40 \times 10^{-5}$	$\text{W m}^{-2}$	SORCE/SOLSTICE
O I 1305 $\text{\AA}$	4.2	$1305.50 \pm 1.75$	$9.14 \times 10^{-5}$	$8.77 \times 10^{-5}$	$1.17 \times 10^{-4}$	$\text{W m}^{-2}$	SORCE/SOLSTICE
Mg II k 2796 $\text{\AA}$	(3.9)	$2796.38 \pm 0.78$	0.0136	0.0135	0.0180	$\text{W m}^{-2}$	SORCE/SOLSTICE
Mg II h 2803 $\text{\AA}$	(3.9)	$2803.48 \pm 0.65$	0.0097	0.0096	0.0126	$\text{W m}^{-2}$	SORCE/SOLSTICE
Cl I 1351 $\text{\AA}$	(3.8)	$1305.50 \pm 1.75$	$9.06 \times 10^{-6}$	$8.57 \times 10^{-6}$	$1.17 \times 10^{-5}$	$\text{W m}^{-2}$	SORCE/SOLSTICE
Ca II K 3934 $\text{\AA}$	(3.8)	$3933.66 \pm 0.50$	0.0114	0.0111	0.0130	$\text{W m}^{-2}$	SORCE/SIM & SOLIS/ISS
Ca II H 3968 $\text{\AA}$	(3.8)	$3968.47 \pm 0.50$	0.0139	0.0139	0.0155	$\text{W m}^{-2}$	SORCE/SIM & SOLIS/ISS
H I 6563 $\text{\AA}$ ( $\text{H}\alpha$ )	(3.8)	$6562.80 \pm 0.50$	0.0369	0.0360	0.0448	$\text{W m}^{-2}$	SORCE/SIM & SOLIS/ISS
Ca II 8542 $\text{\AA}$	(3.8)	$8542.10 \pm 0.50$	0.0347	0.0346	0.0392	$\text{W m}^{-2}$	SORCE/SIM & SOLIS/ISS

**Note.** Listed above the horizontal line are the solar activity proxies, while the rest are the spectral lines and bands whose irradiances are compared with the proxies. F10.7 cm radio flux is registered as both proxy and spectral band. The temperatures of optically thick chromospheric lines are given in parentheses. All irradiances were converted to the values at the distance of 1 au from the Sun.

estimated by fitting a Gaussian function to the distribution of the field strength in each magnetogram, as in Hagenaar (2001). The reductions of magnetic flux due to binning the magnetograms from the original  $4096 \times 4096$  pixels to  $1024 \times 1024$  pixels were 18.9% and 23.9% for the solar maximum (2014 October 23) and minimum (2019 March 1), respectively. Therefore, a typical reduction of 20% is expected to occur.

## 2.2. WDC-SILSO

In 2015, the daily sunspot number was recalibrated and released as a new data set (version 2). We obtained this data set from the WDC-SILSO webpage.<sup>9</sup> Refer to Clette et al. (2014)

for a general account of the sunspot number and recalibrated record.

## 2.3. USAF/NOAA

Since 1977, the areas of sunspot groups were measured and recorded by the US Air Force (USAF) and the National Oceanic and Atmospheric Administration (NOAA),<sup>10</sup> following the record by the Royal Greenwich Observatory. Using this data set, we calculated the daily total sunspot area on the visible hemisphere of the Sun. The sunspot areas are measured in units of millionths of the solar hemisphere (MSH), which is equivalent to  $3 \times 10^6 \text{ km}^2$ .

<sup>9</sup> <https://www.sidc.be/silso/datafiles>

<sup>10</sup> <http://solarcyclescience.com/activerregions.html>

#### 2.4. *SORCE/TIM*

The daily total solar irradiance (TSI) data (level 3, version 19) obtained by the Total Irradiance Monitor (TIM; Kopp et al. 2005) on board the Solar Radiation and Climate Experiment (SORCE; Rottman 2005) were downloaded from the data archive.<sup>11</sup> SORCE operated from 2003 February to 2020 February, which determines the end of the analysis period in this study. However, there are some gaps in observation owing to the degradation of the battery capacity (longest one from August 2013 to February 2014; Woods et al. 2021).

Whereas the TSI increases as the solar activity increases, it is occasionally reduced owing to individual sunspot transit and does not correlate well with other proxies such as the total magnetic flux and total sunspot number. Therefore, the TSI was used for reference purposes only.

#### 2.5. *GOES/XRS*

As one of the X-ray data sets, we analyzed the soft X-ray flux over 1–8 Å, measured by the X-Ray Sensor (XRS) on board the GOES satellite. In this study, we used the daily-averaged “science quality” level 2 data, acquired by the GOES-15 satellite from 2010 May to 2020 February.<sup>12</sup> To determine the noise level, we referred to the value of  $\lesssim 3 \times 10^{-9} \text{ W m}^{-2}$  at  $10^{-5} \text{ W m}^{-2}$  or less provided by Simões et al. (2015).

#### 2.6. *SORCE/XPS and SOLSTICE*

The irradiances of emission lines and bands from X-rays to near-UV were derived using the XUV Photometer System (XPS; Woods & Rottman 2005) and the Solar Stellar Irradiance Comparison Experiment (SOLSTICE; McClintock et al. 2005) on board the SORCE satellite. The data were obtained from the SORCE data archive.

From the XPS daily spectral data (level 4, version 12), which spans over 1 to 400 Å with a spectral resolution of 1 Å, we measured the irradiances of X-rays 5.2–124 Å (ROSAT heritage band), Fe IX 171 Å, Fe X 174 Å, Fe XI 180 Å, Fe XII 193+195 Å (combined), Fe XIV 211 Å, He II 256 Å+blends, Fe XV 284 Å, and He II 304 Å. From the SOLSTICE daily spectral data (level 3, version 18), which covers from 1150 to 3100 Å with a resolution of 1 Å, we estimated the irradiances of C III 1175 Å, Si III 1206 Å, H I 1216 Å (Ly $\alpha$ ), N V 1238 Å, N V 1242 Å, O I 1302 Å, O I 1305 Å, C II 1335 Å, Fe XII 1349 Å, C II 1351 Å, Si IV 1393 Å, Si IV 1402 Å, C IV 1548 Å, C IV 1551 Å, Mg II k 2796 Å, and Mg II h 2803 Å.

In this data set (i.e., SORCE/SOLSTICE daily spectral data: level 3, version 18), the geocoronal effects were removed from Ly $\alpha$ . For each line, we referred to Ayres (2021) for the central wavelength and spectral window to calculate the irradiance and the CHIANTI database for the corresponding formation temperature. All irradiances have been corrected to their respective value at 1 au. The noise levels were estimated by referring to the irradiance uncertainty shown in the data set.

#### 2.7. *Hinode/XRT*

The X-Ray Telescope (XRT; Golub et al. 2007) on board the Hinode satellite captures the full-disk synoptic soft X-ray images roughly twice a day at 6 UT and 18 UT except for the

interruption periods owing to, e.g., CCD bakeout and other engineering operations (Takeda et al. 2016). Montana State University provides the daily-averaged electron temperature ( $T_e$ ), emission measure (EM), and soft X-ray irradiance (5–60 Å) data,<sup>13</sup> which are derived with the filter ratio method based on the isothermal spectrum (5–60 Å) under the assumption of coronal elemental abundance in the CHIANTI atomic database (version 10; Del Zanna et al. 2021).

The filter pairs used for this method are Ti\_poly/Al\_mesh from 2008 February to 2015 May and Al\_poly/Al\_mesh from 2015 June to 2021 June. The correction factors for the stray light and filter contamination are selected to ensure that the  $T_e$  and EM values in the Cycle 24/25 minimum (around 2019) are nearly the same as those in the Cycle 23/24 minimum (around 2008).

Considering the filter ratio method diagnoses the plasmas over a wide temperature range (Narukage et al. 2011), we determined the XRT temperature to be  $\log(T/\text{K}) = 6.2 \pm 0.1$  by taking the average and standard deviation of the  $T_e$  values between 2010 May and 2020 February.

#### 2.8. *F10.7 cm Radio Flux*

The 10.7 cm (2.8 GHz) band radio flux, F10.7 cm, is an excellent proxy of solar activity and has been measured consistently in Canada since 1947 (Tapping 2013). The transparency of the Earth’s atmosphere to this microwave signal makes it possible to monitor solar activity with a high-duty cycle.

In this study, we used the daily F10.7 cm flux data obtained by the Dominion Radio Astrophysical Observatory (DRAO), specifically, the “adjusted” data, which are corrected to the values at 1 au.<sup>14</sup> The data are shown in solar flux units (sfu), which corresponds to  $10^{-22} \text{ W m}^{-2} \text{ Hz}^{-1}$ .

When the Sun is quiet with no flaring activity, the formation of F10.7 cm flux can be described as a combination of thermal radiation from the transition region to the upper chromosphere (temperatures of 20,000–30,000 K), gyroresonance radiation from active regions, and thermal radiation from the active region corona (>1 MK; Gary & Hurford 1994). The variation component, which is used in this study, is mostly due to the active region corona, and hence, we assumed the corresponding temperature to be  $\log(T/\text{K}) \sim 6$ . For the data uncertainties, we assumed that the average error was no more than 0.5% by referring to Tapping & Charrois (1994).

#### 2.9. *SORCE/SIM and SOLIS/ISS*

For the chromospheric lines from the visible to the near-infrared range, we analyzed the daily spectral data of Ca II K 3934 Å, Ca II H 3968 Å, H I 6563 Å (H $\alpha$ ), Ca II 8542 Å, He I 10830 Å measured by the Integrated Sunlight Spectrometer (ISS; Bertello et al. 2011) of the Synoptic Optical Long-term Investigations of the Sun (SOLIS). These spectra are provided as relative intensities with respect to the nearby continuum levels. Therefore, the daily spectral irradiance data of the SORCE’s Spectral Irradiance Monitor (SIM; Harder et al. 2005), level 3, version 27, spanning from 2400 to 24200 Å with a resolution of 10–340 Å, were incorporated to obtain the absolute intensities. Note that the SOLIS/ISS observation was terminated in October 2017.

<sup>11</sup> <https://lasp.colorado.edu/home/sorce/data/>

<sup>12</sup> <https://www.ngdc.noaa.gov/stp/satellite/goes-r.html>

<sup>13</sup> [http://solar.physics.montana.edu/takeda/XRT\\_outgoing/irrad/](http://solar.physics.montana.edu/takeda/XRT_outgoing/irrad/)

<sup>14</sup> <https://www.spaceweather.gc.ca/forecast-prevision/solar-solaire/solarflux/sx-en.php>

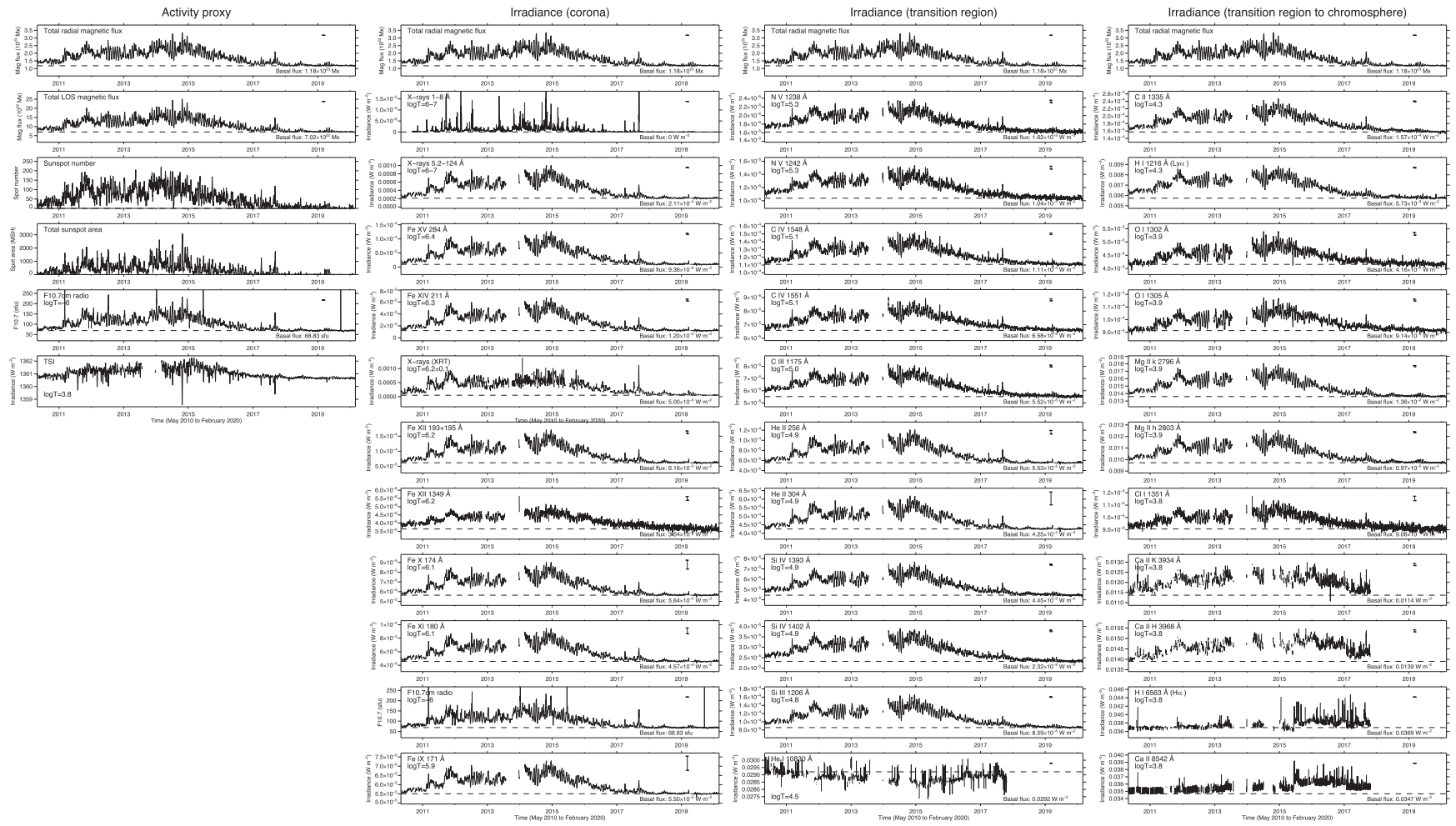


**Figure 1.** Time series of all solar activity proxies (left column) and light curves of all spectral lines and bands (second to fourth columns) analyzed in this study. In each panel, the typical noise level is shown as an error bar on the right. The basal flux is shown as a horizontal dashed line with the value provided at the bottom right.

### 3. Derivation of Power-law Index

#### 3.1. Light Curve

All the daily data used in this study, i.e., the activity proxies and line/band light curves, are shown in Figure 1, whereas the minimum and maximum values of these observables are shown in Table 1. As shown in Figure 1, the irradiance of each line/band varies as the solar activity waxes and wanes. The spikes in the curves indicate that when active regions and other magnetic elements transit across the solar disk, the surface magnetic flux, spot number, and spot area increase (dimming in case of TSI), whereas the EM and irradiances in the Sun's upper atmospheres are enhanced.

In contrast, some lines present weak correlations with solar activity. In particular,  $H\alpha$  and  $\text{Ca II } 8542 \text{ \AA}$  increase brightness only during the declining phase of the cycle, and the long-term trend of  $\text{He I } 10830 \text{ \AA}$  shows an almost inverse correlation with the activity. This may be because these chromospheric lines usually appear in absorption on the disk (Avrett et al. 1994; Brajša et al. 1996).

#### 3.2. Power-law Index

To obtain the scaling relationships between the activity proxies ( $P$ ) and irradiances ( $F$ ), we first obtained the basal fluxes ( $P_0$  and  $F_0$ ) and daily variations (residuals:  $\Delta P = P - P_0$  and  $\Delta F = F - F_0$ ). Then, we created a scatter plot of the residuals for each pair of the proxies and irradiances ( $\Delta F$  versus  $\Delta P$ ). The basal fluxes can be considered as the surface magnetic flux and the resultant magnetically driven high-temperature emissions that are always present as background components. Therefore, they can be measured during the deepest solar minimum. The residuals indicate the appearance of magnetic fields, such as active regions and plages, and the associated heating of the upper atmospheres. Additionally, it is possible to set wide dynamic ranges for scatter plots by taking residuals.

The basal flux was defined as, of the total of 3592 days, from 2010 May to 2020 February, the median of the values on the days that met the following conditions:

1. The final one year, i.e., the deepest solar minimum from 2019 March to 2020 February;
2. When the total sunspot number is 0; and
3. When the radial total unsigned magnetic flux is less than the 10th percentile for the entire period.

As a result, the number of unspotted days that satisfy these conditions was 86. However, depending on the observables, the actual number of unspotted days that was used for taking the medians may differ.

As the observation of SOLIS/ISS was terminated in 2017, for the chromospheric lines observed by this telescope, we considered the median of the 268 days that met the following conditions:

1. One year centered on 2008 December; and
2. When the total sunspot number is 0.

The basal fluxes for all observables are summarized in Table 1 and denoted by horizontal dashed lines in Figure 1. We set the basal fluxes for the total sunspot number, total sunspot area, and the GOES soft X-ray flux (1–8  $\text{\AA}$ ) as 0, 0 MSH, and  $0 \text{ W m}^{-2}$ , respectively.

As described above, the basal flux for each time series was calculated as the median of spotless day data. This is because it is not known whether the minimum value in a time series is truly the lowest value due to data gaps. Therefore, the minimum values in Table 1 are smaller than the basal fluxes in most cases.

Figures 2 to 6 show the scatter plots of irradiances (residual:  $\Delta F$ ) versus the solar activity proxies (residual:  $\Delta P$ ) of radial total unsigned magnetic flux (Figure 2), LOS total unsigned magnetic flux (Figure 3), total sunspot number (Figure 4), total sunspot area (Figure 5), and the F10.7 cm flux (Figure 6). Here, only the data points where both  $\Delta P$  and  $\Delta F$  were positive are plotted. The fractions of data points that were not used due to negative values of  $\Delta P$  or  $\Delta F$  are typically 13%–17% for the SORCE data and 51%–60% for the SOLIS/ISS data.

Each figure shows the result of a linear fit to a double logarithmic plot: The linear fit was applied to the  $(\log \Delta P, \log \Delta F)$  data, where both  $\Delta P$  and  $\Delta F$  were positive, to obtain  $\alpha$  and  $\beta$  as in the following equation:

$$\Delta P = 10^\beta \Delta F^\alpha, \quad (1)$$

or equivalently,

$$\log \Delta P = \beta + \alpha \log \Delta F. \quad (2)$$

We assumed that both  $\log \Delta P$  and  $\log \Delta F$  have errors. Also, we applied a uniform weight for each observable because giving weights to smaller data points allows for wider dynamic ranges over which the linear fit is performed.<sup>15</sup> The degree of dispersion of the data points was also examined by measuring the linear Pearson correlation coefficient,  $\text{CC}(\log \Delta P, \log \Delta F)$ .

It should be noted here that the observation data for which the power-law scalings were calculated are not evenly distributed between 2010 May and 2020 February: there exist observational gaps for each observable as they appear as gaps in the light curves in Figure 1.

### 4. Catalog of Power-law Index

Tables 2–6 summarize the power-law index  $\alpha$ , offset  $\beta$ , correlation coefficient  $\text{CC}$ , number of data points  $N$ , and least-square deviation of the linear fit for all scatter plots in Figures 2–6. The overall trend is that the higher temperature lines and bands show higher CCs. For each line, among different proxies, the total magnetic fluxes and F10.7 cm flux tend to show higher CCs compared to the sunspot number and the area. Because  $\text{He I } 10830 \text{ \AA}$  often falls below its basal flux level (i.e.,  $\Delta F$  often becomes negative), we created scatter plots by taking the absolute value of  $\Delta F$ . For F10.7 cm versus  $\text{Ca II } 8542 \text{ \AA}$  (Figure 6), the scaling factors  $\alpha$  and  $\beta$  are not provided in Table 6 owing to the failure of the linear fit. These chromospheric lines and  $H\alpha$ ,  $\text{Ca II K } 3934 \text{ \AA}$ , and  $\text{Ca II H } 3968 \text{ \AA}$  generally had poorer CCs and least-square deviations.

<sup>15</sup> We also tested the differential weighting method, which puts more weight on larger data. However, the fitting results were not much different from the uniform weighting cases, especially for  $\log \Delta P$  with broad dynamic ranges such as the total radial unsigned magnetic flux. Therefore, we adopted the uniform weighting method in favor of the effective dynamic ranges.

Total unsigned radial magnetic flux

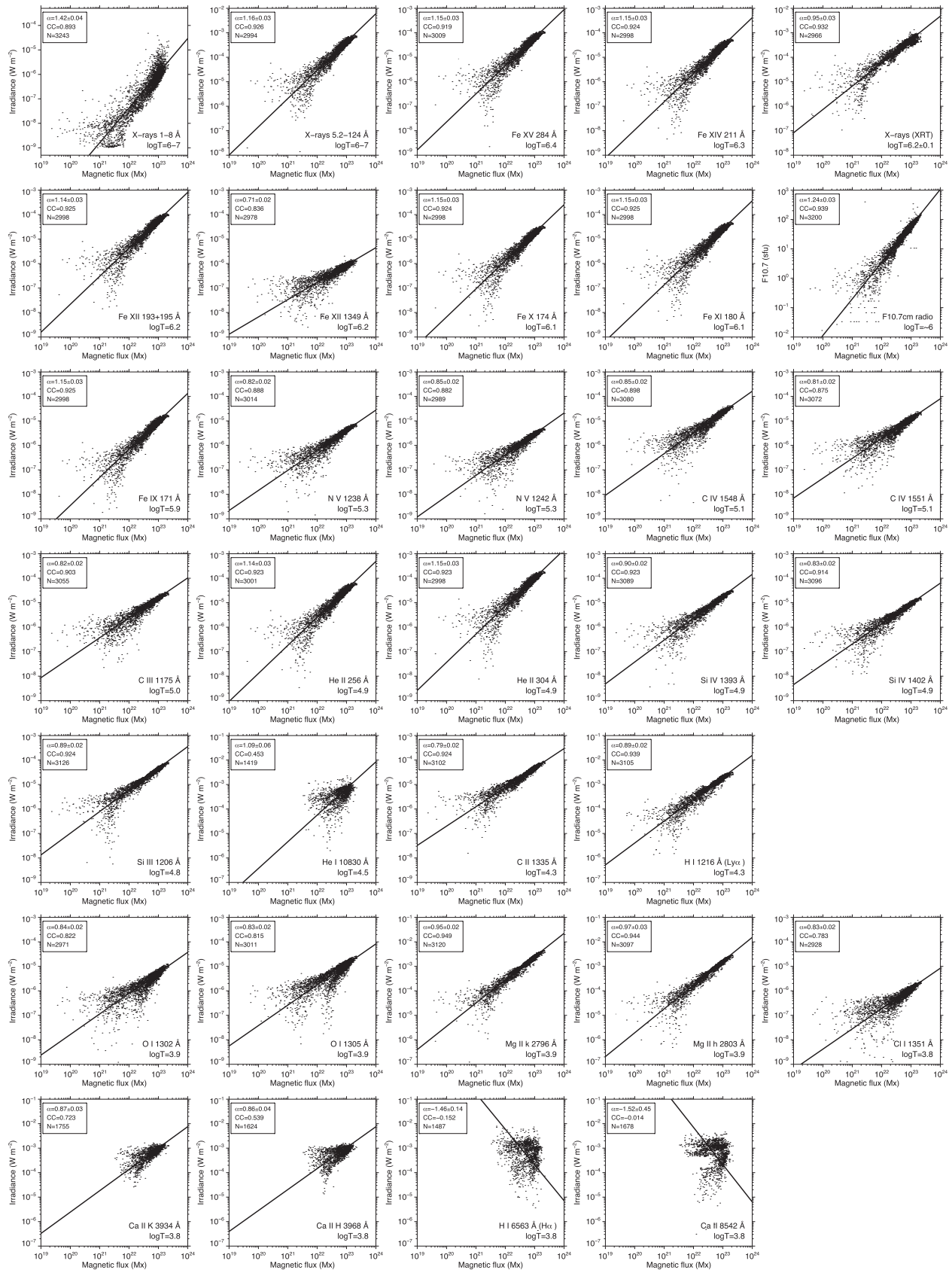


**Figure 2.** Double logarithmic scatter plots of irradiances vs. the total radial unsigned magnetic flux. In each panel, the straight line indicates the result of a linear fitting to the double logarithmic plot. The power-law index  $\alpha$ , correlation coefficient CC, and data number  $N$  are provided at the top left.

Total unsigned LOS magnetic flux

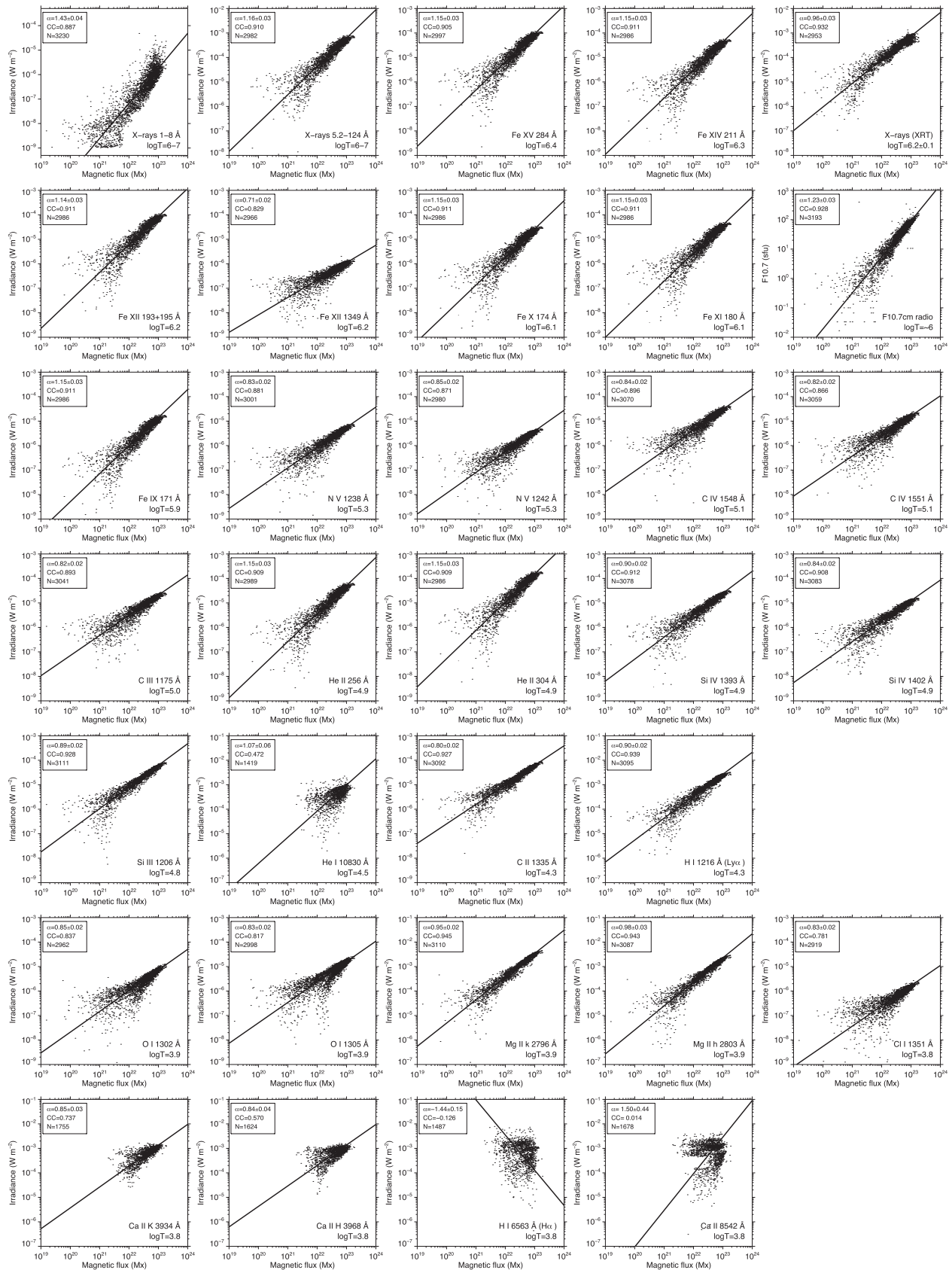


Figure 3. Same as Figure 2 but for the total LOS unsigned magnetic flux.

Total sunspot number

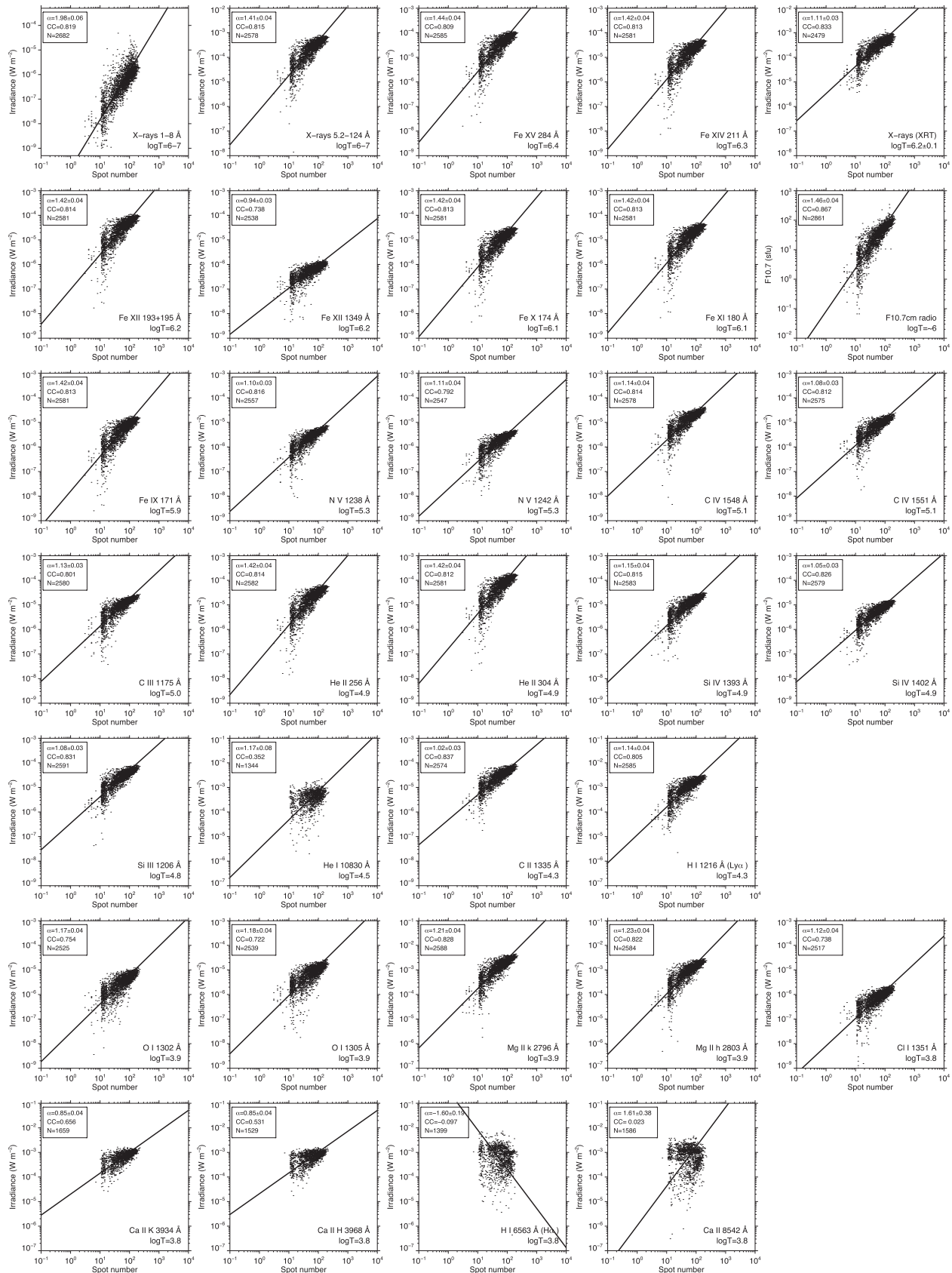


Figure 4. Same as Figure 2 but for the total sunspot number.

Total sunspot area

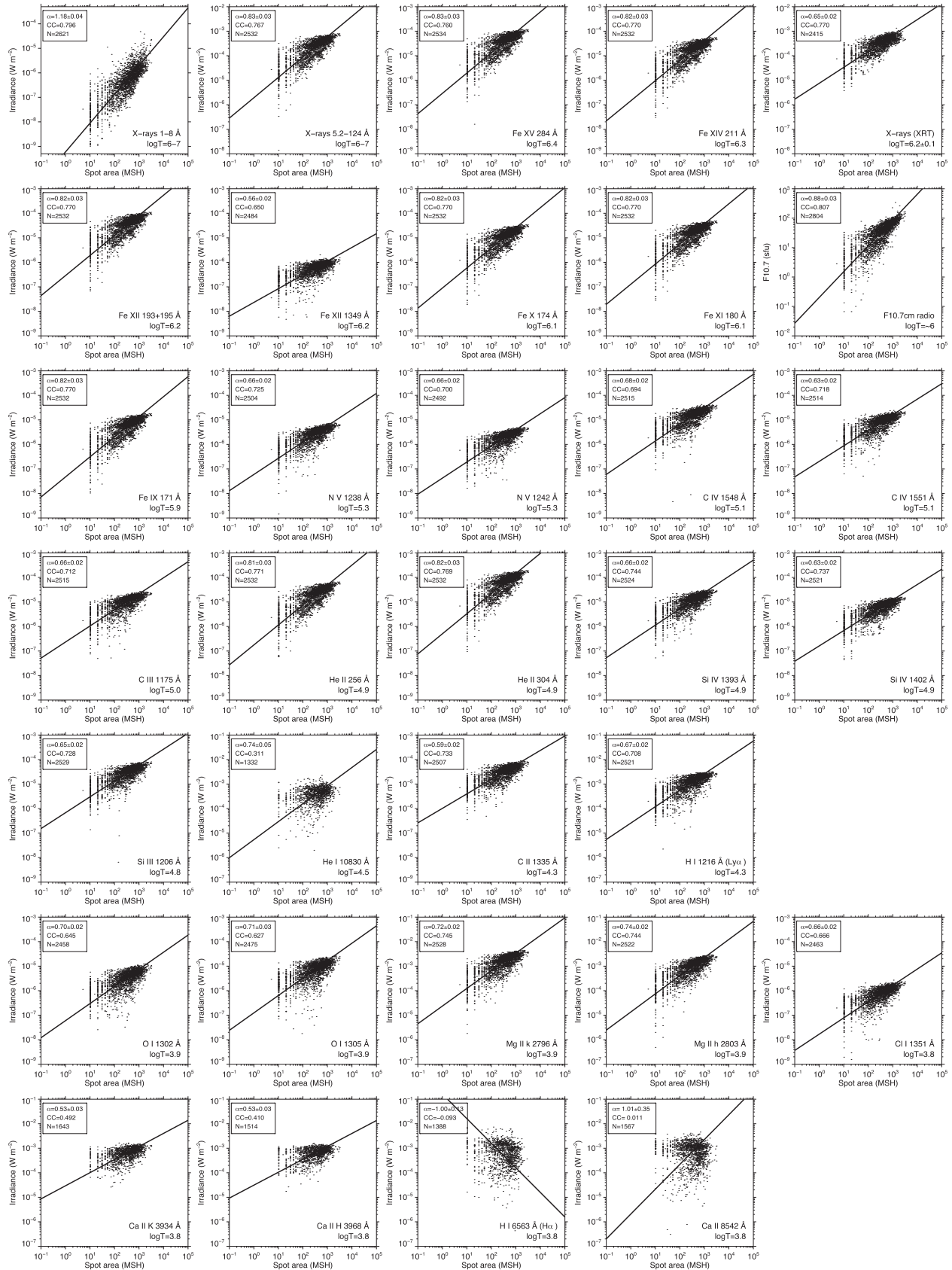


Figure 5. Same as Figure 2 but for the total sunspot area.

F10.7cm radio flux

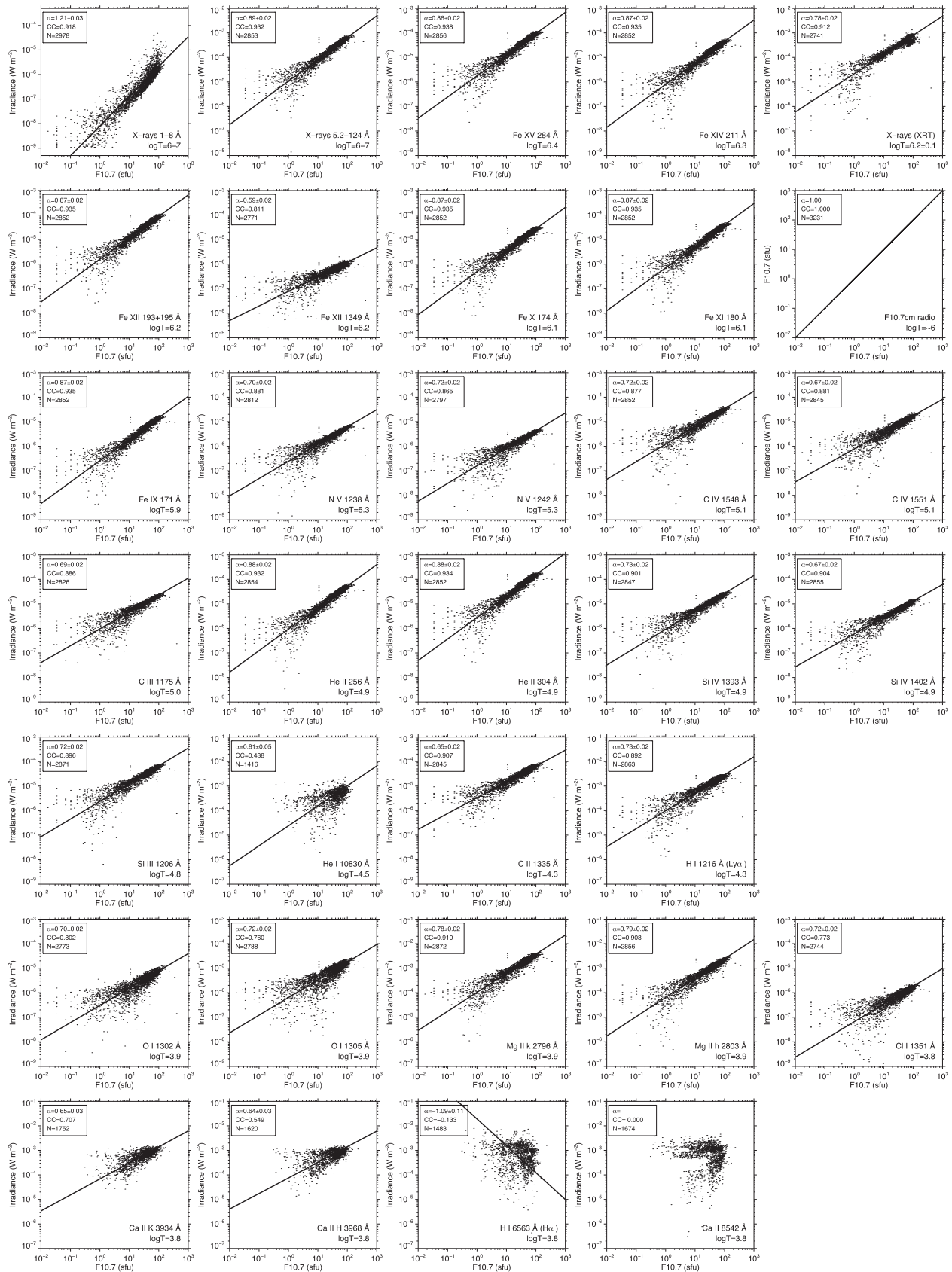


Figure 6. Same as Figure 2 but for the F10.7 cm radio flux.

**Table 2**  
Power-law Indices and Correlations between Irradiance and Total Radial Magnetic Flux

Feature (1)	$\log(T/K)$ (2)	Power-law Index $\alpha$ (3)	Offset $\beta$ (4)	Correlation Coefficient CC (5)	Data Points $N$ (6)	LS Deviation (7)
X-rays 1–8 Å	6–7	$1.42 \pm 0.04$	$-38.6 \pm 0.8$	0.893	3243	0.431
X-rays 5.2–124 Å	6–7	$1.16 \pm 0.03$	$-29.9 \pm 0.7$	0.926	2994	0.247
Fe XV 284 Å	6.4	$1.15 \pm 0.03$	$-30.6 \pm 0.7$	0.919	3009	0.258
Fe XIV 211 Å	6.3	$1.15 \pm 0.03$	$-30.9 \pm 0.7$	0.924	2998	0.248
X-rays (XRT)	$6.2 \pm 0.1$	$0.95 \pm 0.03$	$-25.2 \pm 0.6$	0.932	2966	0.222
Fe XII 193+195 Å	6.2	$1.14 \pm 0.03$	$-30.5 \pm 0.7$	0.925	2998	0.246
Fe XII 1349 Å	6.2	$0.71 \pm 0.02$	$-22.3 \pm 0.5$	0.836	2978	0.236
Fe X 174 Å	6.1	$1.15 \pm 0.03$	$-31.1 \pm 0.7$	0.924	2998	0.248
Fe XI 180 Å	6.1	$1.15 \pm 0.03$	$-30.9 \pm 0.7$	0.925	2998	0.247
F10.7 cm radio	~6	$1.24 \pm 0.03$	$-26.8 \pm 0.7$	0.939	3200	0.225
Fe IX 171 Å	5.9	$1.15 \pm 0.03$	$-31.4 \pm 0.7$	0.925	2998	0.247
N V 1238 Å	5.3	$0.82 \pm 0.02$	$-24.3 \pm 0.5$	0.888	3014	0.233
N V 1242 Å	5.3	$0.85 \pm 0.02$	$-25.1 \pm 0.5$	0.882	2989	0.239
C IV 1548 Å	5.1	$0.85 \pm 0.02$	$-24.2 \pm 0.5$	0.898	3080	0.233
C IV 1551 Å	5.1	$0.81 \pm 0.02$	$-23.6 \pm 0.5$	0.875	3072	0.248
C III 1175 Å	5.0	$0.82 \pm 0.02$	$-23.6 \pm 0.5$	0.903	3055	0.218
He II 256 Å	4.9	$1.14 \pm 0.03$	$-30.8 \pm 0.7$	0.923	3001	0.249
He II 304 Å	4.9	$1.15 \pm 0.03$	$-30.4 \pm 0.7$	0.923	2998	0.250
Si IV 1393 Å	4.9	$0.90 \pm 0.02$	$-25.3 \pm 0.5$	0.923	3089	0.215
Si IV 1402 Å	4.9	$0.83 \pm 0.02$	$-24.1 \pm 0.5$	0.914	3096	0.214
Si III 1206 Å	4.8	$0.89 \pm 0.02$	$-24.7 \pm 0.5$	0.924	3126	0.214
He I 10830 Å	4.5	$1.09 \pm 0.06$	$-28.2 \pm 1.4$	0.453	1419	0.381
C II 1335 Å	4.3	$0.79 \pm 0.02$	$-22.5 \pm 0.5$	0.924	3102	0.193
H I 1216 Å (Ly $\alpha$ )	4.3	$0.89 \pm 0.02$	$-23.3 \pm 0.5$	0.939	3105	0.193
O I 1302 Å	4.2	$0.84 \pm 0.02$	$-24.6 \pm 0.5$	0.822	2971	0.300
O I 1305 Å	4.2	$0.83 \pm 0.02$	$-24.1 \pm 0.5$	0.815	3011	0.307
Mg II k 2796 Å	(3.9)	$0.95 \pm 0.02$	$-24.4 \pm 0.5$	0.949	3120	0.187
Mg II h 2803 Å	(3.9)	$0.97 \pm 0.03$	$-25.2 \pm 0.6$	0.944	3097	0.200
Mg II k+h	(3.9)	$0.96 \pm 0.02$	$-24.5 \pm 0.6$	0.951	3120	0.187
Cl I 1351 Å	(3.8)	$0.83 \pm 0.02$	$-24.9 \pm 0.5$	0.783	2928	0.312
Ca II K 3934 Å	(3.8)	$0.87 \pm 0.03$	$-23.1 \pm 0.8$	0.723	1755	0.214
Ca II H 3968 Å	(3.8)	$0.86 \pm 0.04$	$-22.7 \pm 0.9$	0.539	1624	0.273
H I 6563 Å (H $\alpha$ )	(3.8)	$-1.46 \pm 0.14$	$29.9 \pm 3.1$	-0.152	1487	0.643
Ca II 8542 Å	(3.8)	$-1.52 \pm 0.45$	$31.3 \pm 10.1$	-0.014	1678	0.714

**Note.** The first and second columns show the spectral lines and their formation temperatures, respectively. Columns 3, 4, 5, and 6 provide the power-law index  $\alpha$ , offset  $\beta$ , correlation coefficient CC, and the number of data points  $N$  of each double logarithmic scatter plot of irradiance versus total radial magnetic flux. Column 7 presents the least-square deviation of the linear fit to the double logarithmic plot.

## 5. Dependence of Power-law Index

### 5.1. Temperature Dependence

Figure 7 shows the exponent of irradiances with respect to the total radial unsigned magnetic flux, plotted as a function of temperature. Note that H $\alpha$  and Ca II 8542 Å are omitted because they exhibited negative proportionalities with the magnetic flux (i.e.,  $\alpha < 0$ ). As He I 10830 Å showed an antiphased variation with the activity proxies (Figure 1) and a weak anticorrelation (Table 2), we plotted  $\alpha$  calculated by taking the absolute value of  $\Delta F$ .<sup>16</sup>

Compared to the previous study (Figure 3 in TA22), the increase in the number of observables, especially for the transition region temperatures, allows for scrutinizing the change of  $\alpha$  from the chromosphere to the corona.

For the coronal temperatures,  $\alpha > 1$  for most observables, which is in agreement with many previous studies (see Section 1). However, for Hinode/XRT,  $\alpha$  was slightly below unity owing to several possible reasons. For example, the field

of view of XRT was only about  $2048'' \times 2048''$ , and hence, if there is a bright coronal structure outside the limb, XRT may miss its contribution and underestimate irradiance, especially during the solar maximum. The exclusion of images that contain saturated pixels due to flares may also lead to the underestimation of irradiance. Furthermore, the combination of filters used to create the XRT light curve was changed, making it difficult to compare the long-term evolution. Fe XII 1349 Å also had a coronal formation temperature at  $\log(T/K) = 6.2$ , but  $\alpha$  was well below unity, even smaller than the chromospheric line in the same wavelength range. This may be attributed to the fact that this line is much weaker than the other lines, owing to which the irradiance cannot be easily determined.

The result that the  $\alpha$  values for most chromospheric lines take less than unity also supports the previous analyses (see Section 1). However, it is newly found that most of the transition region lines also take  $\alpha < 1$  as in the chromosphere.

Herein the formation temperature of He I 10830 Å was set to  $\log(T/K) = 4.2$ ; however, it should be noted that this line was formed by the combination of multiple mechanisms (e.g., Andretta & Jones 1997): (1) EUV photons in the corona invade

<sup>16</sup> In this study, we measured the irradiance at the line core of He I 10830 Å and found a weak anticorrelation, while Livingston et al. (2007) showed a strong correlation between its equivalent width and solar activity.

**Table 3**  
Power-law Indices and Correlations between Irradiance and Total LOS Magnetic Flux

Feature (1)	$\log(T/K)$ (2)	Power-law Index $\alpha$ (3)	Offset $\beta$ (4)	Correlation Coefficient CC (5)	Data Points $N$ (6)	LS Deviation (7)
X-rays 1–8 Å	6–7	$1.43 \pm 0.04$	$-38.7 \pm 0.9$	0.887	3230	0.443
X-rays 5.2–124 Å	6–7	$1.16 \pm 0.03$	$-29.8 \pm 0.7$	0.910	2982	0.271
Fe XV 284 Å	6.4	$1.15 \pm 0.03$	$-30.5 \pm 0.7$	0.905	2997	0.279
Fe XIV 211 Å	6.3	$1.15 \pm 0.03$	$-30.8 \pm 0.7$	0.911	2986	0.269
X-rays (XRT)	$6.2 \pm 0.1$	$0.96 \pm 0.03$	$-25.3 \pm 0.6$	0.932	2953	0.221
Fe XII 193+195 Å	6.2	$1.14 \pm 0.03$	$-30.4 \pm 0.7$	0.911	2986	0.267
Fe XII 1349 Å	6.2	$0.71 \pm 0.02$	$-22.3 \pm 0.5$	0.829	2966	0.238
Fe X 174 Å	6.1	$1.15 \pm 0.03$	$-31.0 \pm 0.7$	0.911	2986	0.269
Fe XI 180 Å	6.1	$1.15 \pm 0.03$	$-30.8 \pm 0.7$	0.911	2986	0.268
F10.7 cm radio	~6	$1.23 \pm 0.03$	$-26.3 \pm 0.7$	0.928	3193	0.243
Fe IX 171 Å	5.9	$1.15 \pm 0.03$	$-31.2 \pm 0.7$	0.911	2986	0.268
N V 1238 Å	5.3	$0.83 \pm 0.02$	$-24.3 \pm 0.5$	0.881	3001	0.238
N V 1242 Å	5.3	$0.85 \pm 0.02$	$-24.9 \pm 0.5$	0.871	2980	0.250
C IV 1548 Å	5.1	$0.84 \pm 0.02$	$-23.9 \pm 0.5$	0.896	3070	0.232
C IV 1551 Å	5.1	$0.82 \pm 0.02$	$-23.6 \pm 0.5$	0.866	3059	0.257
C III 1175 Å	5.0	$0.82 \pm 0.02$	$-23.6 \pm 0.5$	0.893	3041	0.228
He II 256 Å	4.9	$1.15 \pm 0.03$	$-30.6 \pm 0.7$	0.909	2989	0.271
He II 304 Å	4.9	$1.15 \pm 0.03$	$-30.4 \pm 0.7$	0.909	2986	0.272
Si IV 1393 Å	4.9	$0.90 \pm 0.02$	$-25.2 \pm 0.5$	0.912	3078	0.229
Si IV 1402 Å	4.9	$0.84 \pm 0.02$	$-24.2 \pm 0.5$	0.908	3083	0.220
Si III 1206 Å	4.8	$0.89 \pm 0.02$	$-24.6 \pm 0.5$	0.928	3111	0.207
He I 10830 Å	4.5	$1.07 \pm 0.06$	$-27.6 \pm 1.3$	0.472	1419	0.374
C II 1335 Å	4.3	$0.80 \pm 0.02$	$-22.6 \pm 0.5$	0.927	3092	0.189
H I 1216 Å (Ly $\alpha$ )	4.3	$0.90 \pm 0.02$	$-23.2 \pm 0.5$	0.939	3095	0.191
O I 1302 Å	4.2	$0.85 \pm 0.02$	$-24.6 \pm 0.5$	0.837	2962	0.288
O I 1305 Å	4.2	$0.83 \pm 0.02$	$-24.0 \pm 0.5$	0.817	2998	0.303
Mg II k 2796 Å	(3.9)	$0.95 \pm 0.02$	$-24.3 \pm 0.6$	0.945	3110	0.194
Mg II h 2803 Å	(3.9)	$0.98 \pm 0.03$	$-25.2 \pm 0.6$	0.943	3087	0.200
Mg II k+h	(3.9)	$0.96 \pm 0.02$	$-24.4 \pm 0.6$	0.947	3109	0.193
Cl I 1351 Å	(3.8)	$0.83 \pm 0.02$	$-24.8 \pm 0.5$	0.781	2919	0.312
Ca II K 3934 Å	(3.8)	$0.85 \pm 0.03$	$-22.5 \pm 0.8$	0.737	1755	0.209
Ca II H 3968 Å	(3.8)	$0.84 \pm 0.04$	$-22.1 \pm 0.9$	0.570	1624	0.264
H I 6563 Å (H $\alpha$ )	(3.8)	$-1.44 \pm 0.15$	$29.2 \pm 3.3$	-0.126	1487	0.653
Ca II 8542 Å	(3.8)	$1.50 \pm 0.44$	$-36.9 \pm 9.9$	0.014	1678	0.714

**Note.** The first and second columns show the spectral lines and their formation temperatures, respectively. Columns 3, 4, 5, and 6 provide the power-law index  $\alpha$ , offset  $\beta$ , correlation coefficient CC, and the number of data points  $N$  of each double logarithmic scatter plot of irradiance versus total LOS magnetic flux. Column 7 presents the least-square deviation of the linear fit to the double logarithmic plot.

the upper chromosphere and photoionize the neutral He atoms. When the generated He ions are recombined, they form a group of He I lines; (2) When electrons with temperatures of 20,000 K or higher collide with the He atoms between the chromosphere and corona, collisional excitation occurs, and as the electrons return to the ground state, He I lines are produced. Therefore, the fact that  $\alpha$  of He I 10830 Å is close to the coronal values (i.e.,  $\alpha > 1$ ) indicates that mechanism (1) is more effective. This may also be related to the fact that the other He lines (He II 256 Å and 304 Å) show  $\alpha$  values that are above unity.

### 5.2. Wavelength Dependence

Figure 8 shows the dependence of the power-law index  $\alpha$  on the spectral line wavelength. As shown in Figure 7, He I 10830 Å was plotted despite its inverse proportionality against the solar activity proxies, while F10.7 cm ( $= 10.7 \times 10^8$  Å) radio flux is shown in the infrared range for visualization purposes only.

As seen in the figure,  $\alpha$  displays a V-shaped profile with the apex located at the near-UV range around 1000–2000 Å. The value increases from below unity to above unity as the wavelength shifts from near-UV both toward the EUV and

X-rays and the infrared and radio waves. This is because the corresponding spectral lines and bands are sensitive to increasingly higher temperature plasmas.

### 6. Applications: Reconstruction of Solar XUV Irradiances

We determined the scaling laws between the solar activity proxies and irradiances of various lines and bands. That is, using the obtained  $\alpha$  and  $\beta$  values, it is possible to calculate the irradiance of these lines/bands from any of these proxies, expressed as:

$$F = 10^{\beta}(P - P_0)^{\alpha} + F_0. \quad (3)$$

We can even estimate the irradiances from proxies for targets having no observation of the upper atmospheres. For example, irradiances can be estimated from surface magnetic field distributions calculated by the solar dynamo models or surface flux transport models, the surface magnetic field distribution acquired by the stellar Zeeman–Doppler imaging, or the starspot sizes estimated from the visible light curve of the Sunlike stars.

XUV irradiance estimates are often based on scaling relationships with other spectral lines or bands (e.g.,

**Table 4**  
Power-law Indices and Correlations between Irradiance and Total Sunspot Number

Feature (1)	$\log(T/K)$ (2)	Power-law Index $\alpha$ (3)	Offset $\beta$ (4)	Correlation Coefficient CC (5)	Data Points $N$ (6)	LS Deviation (7)
X-rays 1–8 Å	6–7	$1.98 \pm 0.06$	$-9.8 \pm 0.1$	0.819	2682	0.419
X-rays 5.2–124 Å	6–7	$1.41 \pm 0.04$	$-6.1 \pm 0.1$	0.815	2578	0.293
Fe XV 284 Å	6.4	$1.44 \pm 0.04$	$-7.0 \pm 0.1$	0.809	2585	0.306
Fe XIV 211 Å	6.3	$1.42 \pm 0.04$	$-7.3 \pm 0.1$	0.813	2581	0.298
X-rays (XRT)	$6.2 \pm 0.1$	$1.11 \pm 0.03$	$-5.5 \pm 0.1$	0.833	2479	0.228
Fe XII 193+195 Å	6.2	$1.42 \pm 0.04$	$-7.0 \pm 0.1$	0.814	2581	0.297
Fe XII 1349 Å	6.2	$0.94 \pm 0.03$	$-7.9 \pm 0.1$	0.738	2538	0.236
Fe X 174 Å	6.1	$1.42 \pm 0.04$	$-7.5 \pm 0.1$	0.813	2581	0.298
Fe XI 180 Å	6.1	$1.42 \pm 0.04$	$-7.4 \pm 0.1$	0.813	2581	0.297
F10.7 cm radio	$\sim 6$	$1.46 \pm 0.04$	$-1.1 \pm 0.1$	0.867	2861	0.258
Fe IX 171 Å	5.9	$1.42 \pm 0.04$	$-7.8 \pm 0.1$	0.813	2581	0.297
N V 1238 Å	5.3	$1.10 \pm 0.03$	$-7.5 \pm 0.1$	0.816	2557	0.232
N V 1242 Å	5.3	$1.11 \pm 0.04$	$-7.7 \pm 0.1$	0.792	2547	0.249
C IV 1548 Å	5.1	$1.14 \pm 0.04$	$-6.9 \pm 0.1$	0.814	2578	0.243
C IV 1551 Å	5.1	$1.08 \pm 0.03$	$-7.0 \pm 0.1$	0.812	2575	0.232
C III 1175 Å	5.0	$1.13 \pm 0.03$	$-7.0 \pm 0.1$	0.801	2580	0.250
He II 256 Å	4.9	$1.42 \pm 0.04$	$-7.2 \pm 0.1$	0.814	2582	0.297
He II 304 Å	4.9	$1.42 \pm 0.04$	$-6.8 \pm 0.1$	0.812	2581	0.299
Si IV 1393 Å	4.9	$1.15 \pm 0.04$	$-7.0 \pm 0.1$	0.815	2583	0.247
Si IV 1402 Å	4.9	$1.05 \pm 0.03$	$-7.1 \pm 0.1$	0.826	2579	0.217
Si III 1206 Å	4.8	$1.08 \pm 0.03$	$-6.5 \pm 0.1$	0.831	2591	0.222
He I 10830 Å	4.5	$1.17 \pm 0.08$	$-5.5 \pm 0.1$	0.352	1344	0.399
C II 1335 Å	4.3	$1.02 \pm 0.03$	$-6.3 \pm 0.1$	0.837	2574	0.205
H I 1216 Å (Ly $\alpha$ )	4.3	$1.14 \pm 0.04$	$-4.9 \pm 0.1$	0.805	2585	0.250
O I 1302 Å	4.2	$1.17 \pm 0.04$	$-7.6 \pm 0.1$	0.754	2525	0.287
O I 1305 Å	4.2	$1.18 \pm 0.04$	$-7.2 \pm 0.1$	0.722	2539	0.310
Mg II k 2796 Å	(3.9)	$1.21 \pm 0.04$	$-5.0 \pm 0.1$	0.828	2588	0.250
Mg II h 2803 Å	(3.9)	$1.23 \pm 0.04$	$-5.2 \pm 0.1$	0.822	2584	0.259
Mg II k+h	(3.9)	$1.23 \pm 0.04$	$-4.8 \pm 0.1$	0.828	2590	0.254
Cl I 1351 Å	(3.8)	$1.12 \pm 0.04$	$-8.1 \pm 0.1$	0.738	2517	0.277
Ca II K 3934 Å	(3.8)	$0.85 \pm 0.04$	$-4.7 \pm 0.1$	0.656	1659	0.218
Ca II H 3968 Å	(3.8)	$0.85 \pm 0.04$	$-4.7 \pm 0.1$	0.531	1529	0.254
H I 6563 Å (H $\alpha$ )	(3.8)	$-1.60 \pm 0.19$	$-0.5 \pm 0.3$	-0.097	1399	0.667
Ca II 8542 Å	(3.8)	$1.61 \pm 0.38$	$-6.0 \pm 0.7$	0.023	1586	0.696

**Note.** The first and second columns show the spectral lines and their formation temperatures, respectively. Columns 3, 4, 5, and 6 provide the power-law index  $\alpha$ , offset  $\beta$ , correlation coefficient CC, and the number of data points  $N$  of each double logarithmic scatter plot of irradiance versus total sunspot number. Column 7 presents the least-square deviation of the linear fit to the double logarithmic plot.

Chamberlin et al. 2007, 2020; Linsky et al. 2014, see also Section 1). However, since the model in this work uses the daily solar activity proxies, although it cannot be used for short timescales like solar and stellar flares, longer-term variations such as rotational modulations and solar cycle variations can be estimated based on more physical relationships, i.e., atmospheric heating owing to surface magnetic field.

To demonstrate this approach, Figure 9 shows the “back-casting” of solar irradiances in the past centuries based on long-term solar observations. In fact, the reconstruction of spectral radiations using historical records has been one of the key scientific targets for understanding the atmospheric/chemical interactions of the Earth and planets (see, e.g., Kopp & Shapiro 2021). Here we used the total spot number (Section 2.2) since 1749 January, total spot area (Section 2.3) since 1874 May, and the F10.7 cm radio flux (Section 2.8) since 1947 February. The irradiances that were reconstructed are those whose scaling laws were verified by a comparison with stellar data in TA22, i.e., X-rays 5.2–124 Å, Fe XV 284 Å, Ly $\alpha$ , and Mg II k 2796 Å. Although it is possible to reconstruct daily irradiances by using the daily proxy data, for better

visualization, we synthesized monthly light curves based on the monthly averaged proxies.

The relative difference between two of the synthesized irradiances is expressed as:

$$d_{\text{TSN,TSA}} = \frac{|F^{\text{TSN}} - F^{\text{TSA}}|}{(F^{\text{TSN}} + F^{\text{TSA}})/2}, \quad (4)$$

$$d_{\text{TSN,F10.7}} = \frac{|F^{\text{TSN}} - F^{\text{F10.7}}|}{(F^{\text{TSN}} + F^{\text{F10.7}})/2}, \quad (5)$$

where  $F^{\text{TSN}}$ ,  $F^{\text{TSA}}$ , and  $F^{\text{F10.7}}$  are the irradiances based on the total sunspot number, total sunspot area, and the F10.7 cm radio flux, respectively. For the period during which the irradiances are derived from multiple proxies, the median values of the relative differences are  $d_{\text{TSN,TSA}} = 14.5\%$  and  $d_{\text{TSN,F10.7}} = 52.9\%$  for X-rays 5.2–124 Å,  $d_{\text{TSN,TSA}} = 22.2\%$  and  $d_{\text{TSN,F10.7}} = 63.7\%$  for Fe XV 284 Å,  $d_{\text{TSN,TSA}} = 4.3\%$  and  $d_{\text{TSN,F10.7}} = 18.6\%$  for Ly $\alpha$ , and  $d_{\text{TSN,TSA}} = 2.7\%$  and  $d_{\text{TSN,F10.7}} = 12.3\%$  for Mg II k 2796 Å. These values, up to approximately 20% for the transition region and chromospheric

**Table 5**  
Power-law Indices and Correlations between Irradiance and Total Sunspot Area

Feature (1)	$\log(T/K)$ (2)	Power-law Index $\alpha$ (3)	Offset $\beta$ (4)	Correlation Coefficient CC (5)	Data Points $N$ (6)	LS Deviation (7)
X-rays 1–8 Å	6–7	$1.18 \pm 0.04$	$-9.2 \pm 0.1$	0.796	2621	0.423
X-rays 5.2–124 Å	6–7	$0.83 \pm 0.03$	$-5.7 \pm 0.1$	0.767	2532	0.317
Fe XV 284 Å	6.4	$0.83 \pm 0.03$	$-6.5 \pm 0.1$	0.760	2534	0.322
Fe XIV 211 Å	6.3	$0.82 \pm 0.03$	$-6.8 \pm 0.1$	0.770	2532	0.311
X-rays (XRT)	$6.2 \pm 0.1$	$0.65 \pm 0.02$	$-5.1 \pm 0.1$	0.770	2415	0.251
Fe XII 193+195 Å	6.2	$0.82 \pm 0.03$	$-6.5 \pm 0.1$	0.770	2532	0.311
Fe XII 1349 Å	6.2	$0.56 \pm 0.02$	$-7.6 \pm 0.0$	0.650	2484	0.263
Fe X 174 Å	6.1	$0.82 \pm 0.03$	$-7.1 \pm 0.1$	0.770	2532	0.311
Fe XI 180 Å	6.1	$0.82 \pm 0.03$	$-6.9 \pm 0.1$	0.770	2532	0.311
F10.7 cm radio	~6	$0.88 \pm 0.03$	$-0.7 \pm 0.1$	0.807	2804	0.297
Fe IX 171 Å	5.9	$0.82 \pm 0.03$	$-7.3 \pm 0.1$	0.770	2532	0.311
N V 1238 Å	5.3	$0.66 \pm 0.02$	$-7.2 \pm 0.1$	0.725	2504	0.276
N V 1242 Å	5.3	$0.66 \pm 0.02$	$-7.4 \pm 0.1$	0.700	2492	0.285
C IV 1548 Å	5.1	$0.68 \pm 0.02$	$-6.5 \pm 0.1$	0.694	2515	0.302
C IV 1551 Å	5.1	$0.63 \pm 0.02$	$-6.7 \pm 0.1$	0.718	2514	0.270
C III 1175 Å	5.0	$0.66 \pm 0.02$	$-6.6 \pm 0.1$	0.712	2515	0.282
He II 256 Å	4.9	$0.81 \pm 0.03$	$-6.8 \pm 0.1$	0.771	2532	0.308
He II 304 Å	4.9	$0.82 \pm 0.03$	$-6.3 \pm 0.1$	0.769	2532	0.312
Si IV 1393 Å	4.9	$0.66 \pm 0.02$	$-6.6 \pm 0.1$	0.744	2524	0.270
Si IV 1402 Å	4.9	$0.63 \pm 0.02$	$-6.8 \pm 0.0$	0.737	2521	0.258
Si III 1206 Å	4.8	$0.65 \pm 0.02$	$-6.2 \pm 0.1$	0.728	2529	0.273
He I 10830 Å	4.5	$0.74 \pm 0.05$	$-5.3 \pm 0.1$	0.311	1332	0.415
C II 1335 Å	4.3	$0.59 \pm 0.02$	$-6.0 \pm 0.0$	0.733	2507	0.245
H I 1216 Å (Ly $\alpha$ )	4.3	$0.67 \pm 0.02$	$-4.6 \pm 0.1$	0.708	2521	0.291
O I 1302 Å	4.2	$0.70 \pm 0.02$	$-7.2 \pm 0.1$	0.645	2458	0.328
O I 1305 Å	4.2	$0.71 \pm 0.03$	$-6.9 \pm 0.1$	0.627	2475	0.346
Mg II k 2796 Å	(3.9)	$0.72 \pm 0.02$	$-4.6 \pm 0.1$	0.745	2528	0.293
Mg II h 2803 Å	(3.9)	$0.74 \pm 0.02$	$-4.9 \pm 0.1$	0.744	2522	0.300
Mg II k+h	(3.9)	$0.73 \pm 0.02$	$-4.4 \pm 0.1$	0.748	2528	0.294
Cl I 1351 Å	(3.8)	$0.66 \pm 0.02$	$-7.8 \pm 0.1$	0.666	2463	0.300
Ca II K 3934 Å	(3.8)	$0.53 \pm 0.03$	$-4.5 \pm 0.1$	0.492	1643	0.262
Ca II H 3968 Å	(3.8)	$0.53 \pm 0.03$	$-4.5 \pm 0.1$	0.410	1514	0.282
H I 6563 Å (H $\alpha$ )	(3.8)	$-1.00 \pm 0.13$	$-0.8 \pm 0.3$	-0.093	1388	0.667
Ca II 8542 Å	(3.8)	$1.01 \pm 0.35$	$-5.7 \pm 0.9$	0.011	1567	0.698

**Note.** The first and second columns show the spectral lines and their formation temperatures, respectively. Columns 3, 4, 5, and 6 provide the power-law index  $\alpha$ , offset  $\beta$ , correlation coefficient CC, and the number of data points  $N$  of each double logarithmic scatter plot of irradiance versus total sunspot area. Column 7 presents the least-square deviation of the linear fit to the double logarithmic plot.

lines and up to approximately 50% for the coronal lines, can be referred to as typical errors when reconstructing irradiances using this method.

Possible sources of errors for this irradiance reconstruction method include the errors in the proxy data (see, Clette et al. 2014, for errors in the sunspot number data) and those in the power-law indices (i.e.,  $\alpha$  and  $\beta$  in Tables 2 to 6). Also, the fact that the power laws were derived only for Cycle 24, which showed a very weak activity, may cause additional errors (see Section 7 for further discussion).

## 7. Summary and Discussion

In this study, we used the methodology described in TA22 to derive the scaling laws between the solar activity proxies (not only the radial magnetic flux but also the LOS flux, total sunspot number, total sunspot area, and the F10.7 cm flux) and the irradiances of various spectral lines and bands. By further increasing the number of lines, especially of the transition region temperatures, we investigated the variation of power-law index  $\alpha$  from the chromospheric to coronal temperatures, as shown in Figure 7.

Our results provide the framework for estimating spectral irradiances from the proxy data. If one of the five proxies is given, one can estimate the line/band irradiances by using the power-law indices  $\alpha$  and offsets  $\beta$  provided in Tables 2–6. For instance, we can estimate the irradiances from the total magnetic flux or total sunspot area of the Sunlike stars obtained from modeling and observations. To demonstrate the usefulness of this method, we reconstructed selected irradiances over the past centuries based on the historical records of solar observations (Figure 9). The relative differences between the synthesized irradiances were up to 20% for the chromospheric and transition region lines and up to 50% for the coronal lines, which can be considered typical errors of the method.

It is also necessary to specify the limitations of this method. The scaling laws were obtained from daily solar synoptic data over the last decade. Therefore, this method can only be applied for reconstructing irradiance variations of timescales longer than a day (i.e., quasi-stationary component) and not for synthesizing transient brightenings, such as solar and stellar flares (timescales of tens of minutes to hours). Additionally, because the last 10 yr was one of the weakest solar activity

**Table 6**  
Power-law Indices and Correlations between Irradiance and F10.7 cm Radio Flux

Feature (1)	$\log(T/K)$ (2)	Power-law Index $\alpha$ (3)	Offset $\beta$ (4)	Correlation Coefficient CC (5)	Data Points $N$ (6)	LS Deviation (7)
X-rays 1–8 Å	6–7	$1.21 \pm 0.03$	$-8.1 \pm 0.0$	0.918	2978	0.334
X-rays 5.2–124 Å	6–7	$0.89 \pm 0.02$	$-5.0 \pm 0.0$	0.932	2853	0.207
Fe XV 284 Å	6.4	$0.86 \pm 0.02$	$-5.8 \pm 0.0$	0.938	2856	0.192
Fe XIV 211 Å	6.3	$0.87 \pm 0.02$	$-6.1 \pm 0.0$	0.935	2852	0.199
X-rays (XRT)	$6.2 \pm 0.1$	$0.78 \pm 0.02$	$-4.7 \pm 0.0$	0.912	2741	0.218
Fe XII 193+195 Å	6.2	$0.87 \pm 0.02$	$-5.8 \pm 0.0$	0.935	2852	0.198
Fe XII 1349 Å	6.2	$0.59 \pm 0.02$	$-7.1 \pm 0.0$	0.811	2771	0.227
Fe X 174 Å	6.1	$0.87 \pm 0.02$	$-6.3 \pm 0.0$	0.935	2852	0.199
Fe XI 180 Å	6.1	$0.87 \pm 0.02$	$-6.2 \pm 0.0$	0.935	2852	0.198
Fe IX 171 Å	5.9	$0.87 \pm 0.02$	$-6.6 \pm 0.0$	0.935	2852	0.198
N V 1238 Å	5.3	$0.70 \pm 0.02$	$-6.6 \pm 0.0$	0.881	2812	0.216
N V 1242 Å	5.3	$0.72 \pm 0.02$	$-6.8 \pm 0.0$	0.865	2797	0.232
C IV 1548 Å	5.1	$0.72 \pm 0.02$	$-5.9 \pm 0.0$	0.877	2852	0.233
C IV 1551 Å	5.1	$0.67 \pm 0.02$	$-6.1 \pm 0.0$	0.881	2845	0.212
C III 1175 Å	5.0	$0.69 \pm 0.02$	$-6.0 \pm 0.0$	0.886	2826	0.207
He II 256 Å	4.9	$0.88 \pm 0.02$	$-6.0 \pm 0.0$	0.932	2854	0.204
He II 304 Å	4.9	$0.88 \pm 0.02$	$-5.6 \pm 0.0$	0.934	2852	0.200
Si IV 1393 Å	4.9	$0.73 \pm 0.02$	$-6.0 \pm 0.0$	0.901	2847	0.209
Si IV 1402 Å	4.9	$0.67 \pm 0.02$	$-6.2 \pm 0.0$	0.904	2855	0.190
Si III 1206 Å	4.8	$0.72 \pm 0.02$	$-5.6 \pm 0.0$	0.896	2871	0.215
He I 10830 Å	4.5	$0.81 \pm 0.05$	$-4.6 \pm 0.1$	0.438	1416	0.386
C II 1335 Å	4.3	$0.65 \pm 0.02$	$-5.5 \pm 0.0$	0.907	2845	0.180
H I 1216 Å (Ly $\alpha$ )	4.3	$0.73 \pm 0.02$	$-4.0 \pm 0.0$	0.892	2863	0.222
O I 1302 Å	4.2	$0.70 \pm 0.02$	$-6.5 \pm 0.0$	0.802	2773	0.283
O I 1305 Å	4.2	$0.72 \pm 0.02$	$-6.2 \pm 0.0$	0.760	2788	0.321
Mg II k 2796 Å	(3.9)	$0.78 \pm 0.02$	$-4.0 \pm 0.0$	0.910	2872	0.214
Mg II h 2803 Å	(3.9)	$0.79 \pm 0.02$	$-4.2 \pm 0.0$	0.908	2856	0.218
Mg II k+h	(3.9)	$0.78 \pm 0.02$	$-3.8 \pm 0.0$	0.914	2868	0.209
Cl I 1351 Å	(3.8)	$0.72 \pm 0.02$	$-7.2 \pm 0.0$	0.773	2744	0.299
Ca II K 3934 Å	(3.8)	$0.65 \pm 0.03$	$-4.2 \pm 0.0$	0.707	1752	0.220
Ca II H 3968 Å	(3.8)	$0.64 \pm 0.03$	$-4.1 \pm 0.0$	0.549	1620	0.271
H I 6563 Å (H $\alpha$ )	(3.8)	$-1.09 \pm 0.11$	$-1.7 \pm 0.2$	-0.133	1483	0.651
Ca II 8542 Å	(3.8)	...	...	0.000	1674	...

**Note.** The first and second columns show the spectral lines and their formation temperatures, respectively. Columns 3, 4, 5, and 6 provide the power-law index  $\alpha$ , offset  $\beta$ , correlation coefficient CC, and the number of data points  $N$  of each double logarithmic scatter plot of irradiance vs. radial F10.7 cm radio flux. Column 7 presents the least-square deviation of the linear fit to the double logarithmic plot.

cycles in the last few 100 yr (e.g., Pesnell 2020), one has to extrapolate the scalings to obtain the irradiances of stronger cycles, as shown in Figure 9.

In addition, irradiances can only be reproduced for stars with almost the same parameters as the current Sun. For example, the chemical abundance is fixed to that of the current Sun, and hence, reproducing irradiances of stars with significantly different abundances can be challenging. Nonetheless, it has been verified by TA22 that the scalings are universal among G-type stars, regardless of age or activity level. Therefore, the method discussed here can be used as far as the irradiance synthesis is conducted for the main-sequence G dwarfs.

Another limitation is that H $\alpha$  and Ca II 8542 Å cannot be reproduced as they brighten only in the declining phase of the solar cycle (Figure 1) and show weak CCs against activity proxies. Based on the Sun-as-a-star monitoring, Maldonado et al. (2019) reported that H $\alpha$  and other Balmer lines (H $\beta$  and H $\gamma$ ) are inversely correlated with the sunspot number and Ca II K intensity. However, these authors only used data over three years. Meunier & Delfosse (2009) analyzed the data for several cycles and showed that although H $\alpha$  and Ca II indices were positively correlated with the activity cycle in the long term, their CCs varied with the phase of the activity cycle. Therefore,

the negative or no correlations for H $\alpha$  and Ca II 8542 Å found in this study may be attributed to the timescale or the activity phase of our sampling. It is also important to analyze spatially resolved data of the Sun to investigate how individual structures such as plagues, filaments, and sunspots affect the chromospheric lines and spectra of the Sun as a whole (e.g., Diercke et al. 2022).

For the active G-type main-sequence stars that emit superflares, Notsu et al. (2019) found a strong positive correlation between the brightness variation amplitude of visible light curves, which is an indicator of the starspot size, and the Ca II 8542 Å and H & K intensities, as opposed to the expectation from this study. It is possible that the solar Ca II 8542 Å line fluxes are in the saturated regime in the atmospheres of solar-like stars, where they only show a weak dependence on the Ca II K intensity (see Figure 5 of Takeda et al. 2012). Cincunegui et al. (2007), who studied various stars ranging from F to M, showed that although H $\alpha$  and Ca II H & K were strongly correlated as a whole, this general trend was lost for individual stars. Reiners et al. (2022) showed that H $\alpha$  in M dwarfs had a positive correlation with the magnetic flux with an exponent of  $\alpha = 1.43$ . However, these authors noted that H $\alpha$  requires a minimum average magnetic field strength of several

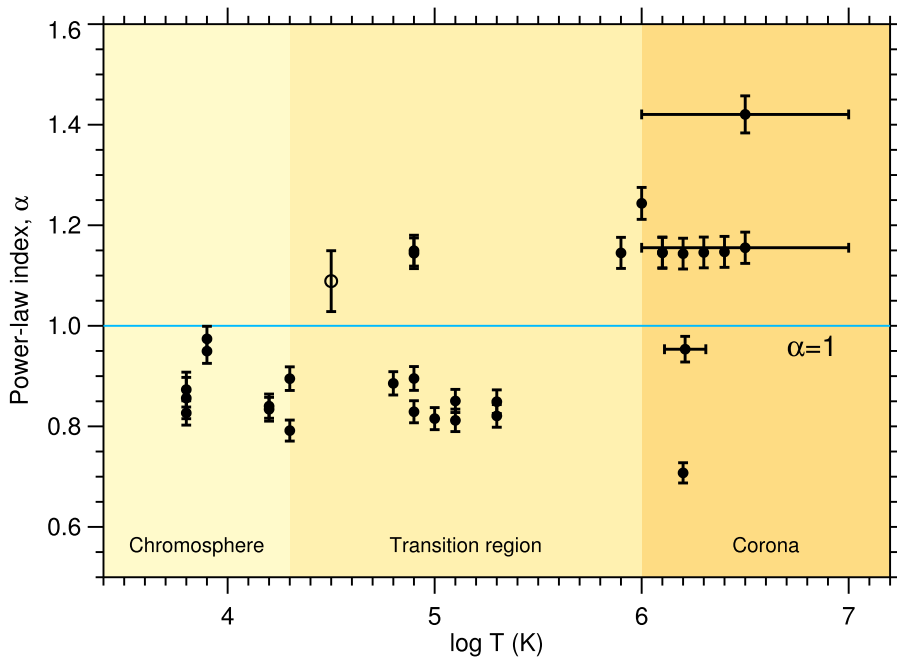


**Figure 7.** Power-law indices  $\alpha$  for the scatter plots of the total radial unsigned magnetic flux and irradiances of various spectral lines/bands (Figure 2 and Table 2), plotted as a function of temperature. Errors in estimating  $\alpha$  are indicated by vertical bars, whereas the horizontal bars show the temperature ranges for the three X-ray data, GOES/XRS 1–8 Å, SORCE/XPS 5.2–124 Å, and Hinode/XRT 5–60 Å. He I 10830 Å, which shows an inverse proportionality against activity proxies, is indicated by an open circle. The  $\alpha = 1$  level is indicated by a sky-blue line.

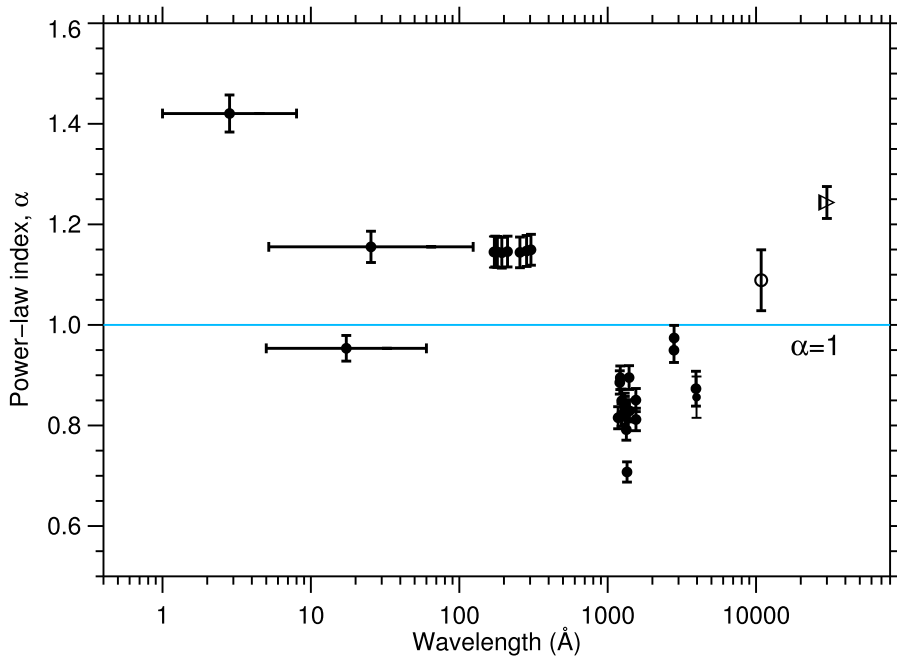


**Figure 8.** Same as Figure 7 but plotted as a function of wavelength. He I 10830 Å, which shows an inverse proportionality against activity proxies, is indicated by an open circle. F10.7 cm radio flux, which corresponds to the wavelength of  $10.7 \times 10^8$  Å, is indicated by the open right-facing triangle at the rightmost end.

hundred G to ensure a detectable emission. Therefore, the chromospheric lines that appear in absorption on the Sun may have different formation mechanisms compared to the chromospheres of active stars. One possible explanation of this difference can be attributed to the frequency of occurrence of coronal flare events in active stars, which can heat the chromosphere via electron beams and excite hydrogen line emissions. In contrast, frequent solar microflares can mostly heat the transition region and do not contribute much to chromospheric heating.

This points to the importance of estimating spectral irradiances using the scaling laws as well as examining the relationships between starspots and the upper atmospheric variations by actually conducting long-term monitoring of stars at multiple wavelengths. To this end, Toriumi et al. (2020) proposed the methodology of estimating the size of stellar active regions by acquiring the light curves for many different rotational phases, not only in the visible band but also in the XUV band. Recently, it has become possible to track the growth of starspots based on the long-term changes of dips in

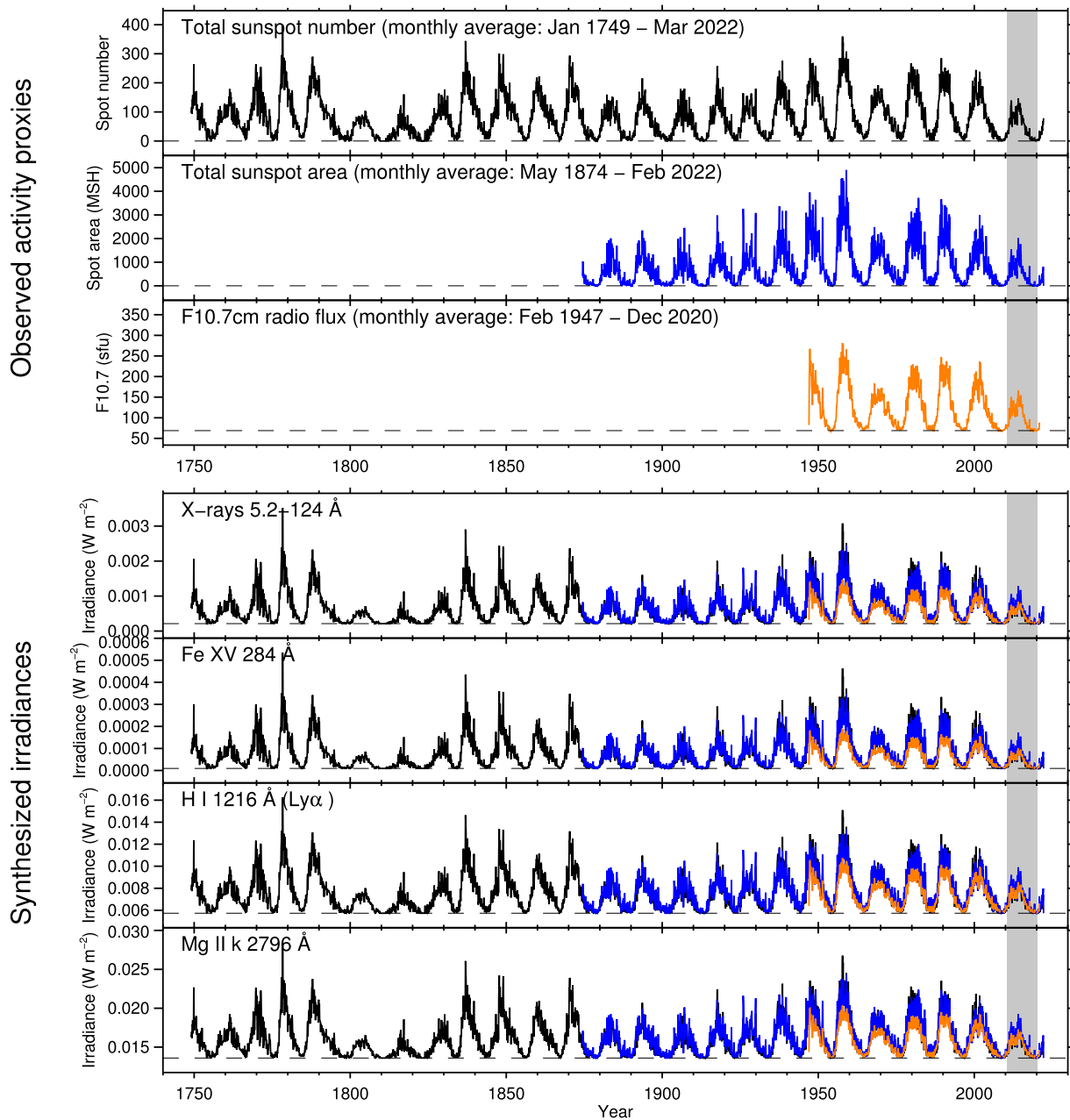


**Figure 9.** Reconstruction of irradiances over the past centuries using the historical records of activity proxy observations. The top three rows are the monthly averaged total sunspot number, total sunspot area, and the F10.7 cm radio flux. The four remaining rows are the synthesized X-rays 5.2–124 Å, Fe XV 284 Å, Ly $\alpha$ , and Mg II k 2796 Å. The black, blue, and orange curves indicate the monthly data synthesized based on the sunspot number (top row), spot area (second row), and the F10.7 cm flux (third row), respectively. The basal fluxes are shown as horizontal dashed lines. The gray hatch indicates the period during which the scalings between the proxies and irradiances are measured in this study (2010 May to 2020 February).

stellar visible light curves and the starspot mapping technique (Namekata et al. 2019, 2020); however, if there is contemporaneous XUV observation, we can also obtain clues to understand how active region atmospheres evolve. For instance, whether the rotational modulations of visible light and H $\alpha$  are correlated, uncorrelated, or anticorrelated is a key to probing the chromospheric activity of starspots (Maehara et al. 2021; Namekata et al. 2022; Schöfer et al. 2022), which should be expanded to the XUV range.

In this study, we derived the scaling laws between the solar activity proxies and the irradiances. However, the mutual relations between irradiances of different spectral lines may also be utilized to investigate the physical processes of the solar

and stellar atmospheres (e.g., Linsky et al. 2014, 2020; Youngblood et al. 2017; France et al. 2018). In TA22, the power-law indices were also obtained by dividing the total 10-year period into four phases according to the solar activity, and it was found that  $\alpha$  was smallest during the cycle maximum and largest during the minimum. Although the  $\alpha$  values were derived only for the entire 10 yr period in this study, it is possible that  $\alpha$  depends on the activity phase, and this may cause differences between the Sun and other stars. Future studies on such mutual relations and cycle dependence are expected.

Another possible direction is to reconstruct the XUV irradiances using radio fluxes. Currently, observations of the

radio photosphere are performed for a limited sample of G-type stars (Villadsen et al. 2014). However, the next generation Very Large Array (ngVLA) can supposedly detect radio photospheres of many more main-sequence stars (Carilli et al. 2019). In this study, strong correlations were found between the F10.7 cm (2.8 GHz) radio flux and the XUV irradiances, which indicates that the radio fluxes can be useful proxies for reconstructing stellar XUV line fluxes.

Understanding the basal fluxes requires further investigations. For the late-type stars, Schrijver (1987) found the power-law scalings of the X-ray emission with the Ca II and Mg II emissions by subtracting the basal fluxes for the chromospheric lines. Schrijver (1987) interpreted the basal fluxes as a component due to pure acoustic heating of an unmagnetized atmosphere. In this study, however, we defined the basal fluxes as the medians of unspotted values in the minimum of the solar activity cycle and, by subtracting the basal fluxes from the light curves, we derived the power-law scalings. Magnetic fluxes are ubiquitously distributed even in the quiet Sun during the cycle minimum, causing the atmospheric heating above. Therefore, in this study, the basal fluxes can be represented by the minimum magnetic flux and associated heating (Schröder et al. 2012). This view may be supported by the fact that nonthermal broadening is detected for the chromospheric and transition region lines during the cycle minimum (e.g., Ayres et al. 2021; for further discussions, see Testa et al. 2015; Linsky 2019).

In TA22 and this study, the scalings were examined only for selected lines and bands of the chromospheric to coronal temperatures. However, it is important to extend these relations for the continuum components by evaluating the scaling relationships between the entire XUV spectrum and the activity proxies, such as the total magnetic flux, for every single wavelength bin, including the continuum, rather than extracting the emission lines only. This would make it possible to reconstruct the whole XUV spectra for the F-, G-, and K-type stars. Radiative energy distributions over the wavelength for planet-hosting stars can provide critical information for assessing the efficiency of atmospheric escape from the (exo) planets orbiting them. Derivation of such scalings requires further analysis that we defer to forthcoming publications.

The authors acknowledge the comments suggested by the referee, which helped to improve the quality of the paper. The authors would like to thank Dr. Aki Takeda for the useful comments on the XRT synoptic data. Data are courtesy of the science teams of SDO, WDC-SILSO, USAF/NOAA, SORCE, GOES, Hinode, DRAO, and SOLIS. HMI is an instrument on board SDO, a mission for NASA's Living With a Star program. Hinode is a Japanese mission developed and launched by ISAS/JAXA, collaborating with NAOJ as a domestic partner, NASA and STFC (UK) as international partners. Scientific operation of the Hinode mission is conducted by the Hinode science team organized at ISAS/JAXA. This team mainly consists of scientists from institutes in the partner countries. Support for the post-launch operation is provided by JAXA and NAOJ (Japan), STFC (U.K.), NASA, ESA, and NSC (Norway). ISS data were acquired by SOLIS instruments operated by NISP/NSO/AURA/NSF. This work was supported by JSPS KAKENHI Grant Nos. JP20KK0072 (PI: S. Toriumi), JP21H01124 (PI: T. Yokoyama), JP21H04492 (PI: K. Kusano), JP21J00316 (PI: K. Namekata), and JP21J00106 (PI: Y. Notsu). V.S.A. was supported by the GSFC Sellers

Exoplanet Environments Collaboration (SEEC), which is funded by the NASA Planetary Science Division's Internal Scientist Funding Model (ISFM), NASA's TESS Cycle 1, HST Cycle 27, and NICER Cycle 2 project funds.

## ORCID iDs

Shin Toriumi  <https://orcid.org/0000-0002-1276-2403>

Vladimir S. Airapetian  <https://orcid.org/0000-0003-4452-0588>

Kosuke Namekata  <https://orcid.org/0000-0002-1297-9485>

Yuta Notsu  <https://orcid.org/0000-0002-0412-0849>

## References

- Airapetian, V. S., Barnes, R., Cohen, O., et al. 2020, *IJAsB*, **19**, 136
- Andretta, V., & Jones, H. P. 1997, *ApJ*, **489**, 375
- Avrett, E. H., Fontenla, J. M., & Loeser, R. 1994, in IAU Symp. 154, *Infrared Solar Physics*, ed. D. M. Rabin, J. T. Jefferies, & C. Lindsey (Dordrecht: Kluwer), 35
- Ayres, T., De Pontieu, B., & Testa, P. 2021, *ApJ*, **916**, 36
- Ayres, T. R. 2020, *ApJS*, **250**, 16
- Ayres, T. R. 2021, *ApJ*, **908**, 205
- Barczynski, K., Peter, H., Chitta, L. P., & Solanki, S. K. 2018, *A&A*, **619**, A5
- Benz, A. O. 2017, *LRSP*, **14**, 2
- Benz, A. O., & Güdel, M. 2010, *ARA&A*, **48**, 241
- Berdugina, S. V. 2005, *LRSP*, **2**, 8
- Bertello, L., Pevtsov, A. A., Harvey, J. W., & Toussaint, R. M. 2011, *SoPh*, **272**, 229
- Bražša, R., Pohjolainen, S., Ruždjak, V., et al. 1996, *SoPh*, **163**, 79
- Brun, A. S., & Browning, M. K. 2017, *LRSP*, **14**, 4
- Carilli, C., Butler, B., Golap, K., Carilli, M. T., & White, S. M. 2019, *BAAS*, **51**, 243
- Chadney, J. M., Galand, M., Unruh, Y. C., Koskinen, T. T., & Sanz-Forcada, J. 2015, *Icar*, **250**, 357
- Chamberlin, P. C., Eparvier, F. G., Knoer, V., et al. 2020, *SpWea*, **18**, e02588
- Chamberlin, P. C., Woods, T. N., & Eparvier, F. G. 2007, *SpWea*, **5**, S07005
- Charbonneau, P. 2020, *LRSP*, **17**, 4
- Chen, P. F. 2011, *LRSP*, **8**, 1
- Cheung, M. C. M., & Isobe, H. 2014, *LRSP*, **11**, 3
- Cincunegui, C., Díaz, R. F., & Mauas, P. J. D. 2007, *A&A*, **469**, 309
- Clette, F., Svalgaard, L., Vaquero, J. M., & Cliver, E. W. 2014, *SSRv*, **186**, 35
- Collier Cameron, A., & Robinson, R. D. 1989, *MNRAS*, **238**, 657
- Cruddace, R., Paresce, F., Bowyer, S., & Lampton, M. 1974, *ApJ*, **187**, 497
- Davenport, J. R. A. 2016, *ApJ*, **829**, 23
- Del Zanna, G., Dere, K. P., Young, P. R., & Landi, E. 2021, *ApJ*, **909**, 38
- Diercke, A., Kuckein, C., Cauley, P. W., et al. 2022, *A&A*, **661**, A107
- Fan, Y. 2021, *LRSP*, **18**, 5
- Fisher, G. H., Longcope, D. W., Metcalf, T. R., & Pevtsov, A. A. 1998, *ApJ*, **508**, 885
- Fletcher, L., Dennis, B. R., Hudson, H. S., et al. 2011, *SSRv*, **159**, 19
- France, K., Arulanandham, N., Fossati, L., et al. 2018, *ApJS*, **239**, 16
- Gary, D. E., & Hurford, G. J. 1994, *ApJ*, **420**, 903
- Golub, L., Deluca, E., Austin, G., et al. 2007, *SoPh*, **243**, 63
- Güdel, M. 2004, *A&ARv*, **12**, 71
- Güdel, M. 2007, *LRSP*, **4**, 3
- Hagenaar, H. J. 2001, *ApJ*, **555**, 448
- Harder, J., Lawrence, G., Fontenla, J., Rottman, G., & Woods, T. 2005, *SoPh*, **230**, 141
- Harra, L. K., Schrijver, C. J., Janvier, M., et al. 2016, *SoPh*, **291**, 1761
- Harvey, K. L., & White, O. R. 1999, *ApJ*, **515**, 812
- Johnstone, C. P., Bartel, M., & Güdel, M. 2021, *A&A*, **649**, A96
- Klimchuk, J. A. 2006, *SoPh*, **234**, 41
- Kopp, G., Lawrence, G., & Rottman, G. 2005, *SoPh*, **230**, 129
- Kopp, G., & Shapiro, A. 2021, *SoPh*, **296**, 60
- Linsky, J. 2019, *Host Stars and their Effects on Exoplanet Atmospheres: An Introductory Overview* (Cham: Springer)
- Linsky, J. L., Fontenla, J., & France, K. 2014, *ApJ*, **780**, 61
- Linsky, J. L., Wood, B. E., Youngblood, A., et al. 2020, *ApJ*, **902**, 3
- Livingston, W., Wallace, L., White, O. R., & Giampapa, M. S. 2007, *ApJ*, **657**, 1137
- Maehara, H., Notsu, Y., Namekata, K., et al. 2021, *PASJ*, **73**, 44
- Maehara, H., Shibayama, T., Notsu, S., et al. 2012, *Natur*, **485**, 478
- Maldonado, J., Phillips, D. F., Dumusque, X., et al. 2019, *A&A*, **627**, A118

- McClintock, W. E., Rottman, G. J., & Woods, T. N. 2005, *SoPh*, 230, 225
- Meunier, N., & Delfosse, X. 2009, *A&A*, 501, 1103
- Namekata, K., Davenport, J. R. A., Morris, B. M., et al. 2020, *ApJ*, 891, 103
- Namekata, K., Maehara, H., Honda, S., et al. 2021, *NatAs*, 6, 241
- Namekata, K., Maehara, H., Honda, S., et al. 2022, *ApJL*, 926, L5
- Namekata, K., Maehara, H., Notsu, Y., et al. 2019, *ApJ*, 871, 187
- Narukage, N., Sakao, T., Kano, R., et al. 2011, *SoPh*, 269, 169
- Notsu, Y., Maehara, H., Honda, S., et al. 2019, *ApJ*, 876, 58
- Noyes, R. W., Weiss, N. O., & Vaughan, A. H. 1984, *ApJ*, 287, 769
- Pesnell, W. D. 2020, *JSWSC*, 10, 60
- Pevtsov, A. A., Fisher, G. H., Acton, L. W., et al. 2003, *ApJ*, 598, 1387
- Pizzolato, N., Maggio, A., Micela, G., Sciortino, S., & Ventura, P. 2003, *A&A*, 397, 147
- Reiners, A., Schüssler, M., & Passegger, V. M. 2014, *ApJ*, 794, 144
- Reiners, A., Shulyak, D., Käpylä, P. J., et al. 2022, *A&A*, 662, A41
- Rezaei, R., Schlichenmaier, R., Beck, C. A. R., Bruls, J. H. M. J., & Schmidt, W. 2007, *A&A*, 466, 1131
- Rottman, G. 2005, *SoPh*, 230, 7
- Sanz-Forcada, J., Micela, G., Ribas, I., et al. 2011, *A&A*, 532, A6
- Scherrer, P. H., Schou, J., Bush, R. I., et al. 2012, *SoPh*, 275, 207
- Schröfer, P., Jeffers, S. V., Reiners, A., et al. 2022, *A&A*, 663, A68
- Schou, J., Scherrer, P. H., Bush, R. I., et al. 2012, *SoPh*, 275, 229
- Schrijver, C. J. 1987, *A&A*, 172, 111
- Schrijver, C. J., Cote, J., Zwaan, C., & Saar, S. H. 1989, *ApJ*, 337, 964
- Schröder, K. P., Mittag, M., Pérez Martínez, M. I., Cuntz, M., & Schmitt, J. H. M. M. 2012, *A&A*, 540, A130
- Shibata, K., & Magara, T. 2011, *LRSP*, 8, 6
- Shoda, M., & Takasao, S. 2021, *A&A*, 656, A111
- Simões, P. J. A., Hudson, H. S., & Fletcher, L. 2015, *SoPh*, 290, 3625
- Skumanich, A. 1972, *ApJ*, 171, 565
- Skumanich, A., Smythe, C., & Frazier, E. N. 1975, *ApJ*, 200, 747
- Solanki, S. K. 2003, *A&ARv*, 11, 153
- Strassmeier, K. G. 2009, *A&ARv*, 17, 251
- Takasao, S., Mitsuishi, I., Shimura, T., et al. 2020, *ApJ*, 901, 70
- Takeda, A., Yoshimura, K., & Saar, S. H. 2016, *SoPh*, 291, 317
- Takeda, Y., Tajitsu, A., Honda, S., et al. 2012, *PASJ*, 64, 130
- Tapping, K. F. 2013, *SpWea*, 11, 394
- Tapping, K. F., & Charrois, D. P. 1994, *SoPh*, 150, 305
- Testa, P., Saar, S. H., & Drake, J. J. 2015, *RSPTA*, 373, 20140259
- Toriumi, S. 2014, *PASJ*, 66, S6
- Toriumi, S., & Airapetian, V. S. 2022, *ApJ*, 927, 179
- Toriumi, S., Airapetian, V. S., Hudson, H. S., et al. 2020, *ApJ*, 902, 36
- Toriumi, S., Schrijver, C. J., Harra, L. K., Hudson, H., & Nagashima, K. 2017, *ApJ*, 834, 56
- Toriumi, S., & Wang, H. 2019, *LRSP*, 16, 3
- Veronig, A. M., Odert, P., Leitzinger, M., et al. 2021, *NatAs*, 5, 697
- Vidotto, A. A. 2021, *LRSP*, 18, 3
- Vidotto, A. A., Gregory, S. G., Jardine, M., et al. 2014, *MNRAS*, 441, 2361
- Villadsen, J., Hallinan, G., Bourke, S., Güdel, M., & Rupen, M. 2014, *ApJ*, 788, 112
- Woods, T. N., Harder, J. W., Kopp, G., et al. 2021, *SoPh*, 296, 127
- Woods, T. N., & Rottman, G. 2005, *SoPh*, 230, 375
- Wright, N. J., Drake, J. J., Mamajek, E. E., & Henry, G. W. 2011, *ApJ*, 743, 48
- Youngblood, A., France, K., Loyd, R. O. P., et al. 2016, *ApJ*, 824, 101
- Youngblood, A., France, K., Loyd, R. O. P., et al. 2017, *ApJ*, 843, 31
- Zhuleku, J., Warnecke, J., & Peter, H. 2020, *A&A*, 640, A119